Preprint

Title: **Automated Detection of Slow Slip Events from InSAR: Application to the North Anatolian Fault**

Authors: Estelle Neyrinck, Baptiste Rousset, Cécile Doubre and Luis Rivera

Affiliation: ITES, CNRS, Université de Strasbourg, Strasbourg, France

Automated Detection of Slow Slip Events from InSAR: Application to the North Anatolian Fault

Estelle Neyrinck[1], Baptiste Rousset[1], Cécile Doubre[1], Luis Rivera[1]

[1]ITES, CNRS, Université de Strasbourg, Strasbourg, France

Key Points:

- We developed a geodetic matched filter approach on InSAR data that enables to detect shallow slow slip events along strike-slip faults.
- Based on synthetic tests, it can detect shallow events larger than M_w 4.5 with 90 % confidence using horizontal East-West time series.
- Application along creeping segments of the North Anatolian Fault validates the method by detecting and characterizing five slow slip events.

Corresponding author: Estelle Neyrinck, `eneyrinck@unistra.fr`

Abstract

The growing volume of InSAR time series offers new opportunities to systematically detect transient aseismic deformation, but identifying low-amplitude slow slip events (SSEs) remains challenging due to noise and limited temporal resolution. Here, we adapt the geodetic matched filter, originally developed for GNSS data, to InSAR displacement time series in the context of shallow strike-slip faults. The method relies on correlations between physics-based templates and relative displacement time series constructed between pixels located on either side of the fault, enhancing the signal-to-noise ratio and mitigating atmospheric artifacts. Using synthetic experiments with realistic noise, we quantify detection thresholds and show that SSEs with magnitudes as small as M_w 4–4.5 can be reliably detected at shallow depths. A validation strategy based on spatial coherence and weighted stacking of displacement time series significantly reduces false detections. We apply this approach to the Izmit and Ismetpasa segments of the North Anatolian Fault using multi-level processed InSAR datasets. The method successfully retrieves previously documented SSEs and shows that advanced post-processing improves detection capability. Detected events have magnitudes M_w 4.0–4.3, shallow depths ($<$ 2–4 km), and durations of days to weeks, consistent with independent geodetic observations. These results demonstrate that physics-based template matching provides a robust and scalable framework for automatic SSE detection in InSAR time series.

Plain Language Summary

Active faults do not only produce sudden earthquakes. They can also slip slowly without generating seismic waves. These "slow slip events" are important because their occurrence changes our view of the seismic cycle and our understanding of the interseismic loading period, influencing seismic hazard estimates. In recent years, satellite radar measurements have greatly improved our ability to quantify small amplitude ground deformations over large areas. However, the growing volume of data requires automatic methods to identify slow slip events. In this study, we adapt a detection method originally developed for GNSS data to InSAR time series. The method compares satellite observations with physics-based models of fault slip to identify signals consistent with SSEs, even when they are close to the noise level. Tests with realistic synthetic data show that the approach can detect shallow events larger than magnitude 4.5 with at least 90% confidence, and events larger than magnitude 4.25 with moderate confidence. We applied the method to two creeping segments of the North Anatolian Fault between 2016 and 2021. It successfully detected several previously reported slow slip events without prior information. This approach could help rapidly detect and characterize transient slow slip events along active strike-slip faults worldwide.

1 Introduction

Since the first observations of aseismic creep along the San Andreas Fault (SAF) by Steinbrugge et al. (1960), numerous observations have been made worldwide, refining our understanding of the seismic cycle and its implications for seismic hazard estimates (Avouac, 2015). Due to the increase in geodetic measurements and improvements in their temporal resolution, the intermittent occurrence of aseismic slip has been documented in several tectonic contexts, including subduction zones and strike-slip faults (Bürgmann, 2018). In subduction zones, large transient slow slip events (SSEs) of M_w up to 7.5 and producing up to several centimeters of surface displacement, are mostly detected with Global Navigation Satellite System (GNSS) observations (Dragert et al., 2001), although strainmeters (Hawthorne & Rubin, 2013) and tiltmeters (Hirose & Obara, 2005) can also capture them. Along strike-slip faults, most observed SSEs occur in the shallow parts of faults, producing surface deformation footprints only a few kilometers wide with centimetric displacements. Whereas creepmeters can detect SSEs with millimeter-scale offsets at specific locations (Linde et al., 1996; Bilham et al., 2016), Interferometric Synthetic Aperture Radar (InSAR) time series have also proven valuable for detecting shallow SSEs along strike-slip faults (e.g. Rousset et al., 2016; Materna et al., 2024).

Developing automatic - or quasi-automatic - methods for SSE detection along strike-slip faults is essential to cope with the rapidly growing volume of InSAR measurements and to densify worldwide SSE catalogs. Several approaches have been proposed to extract transient deformation in geodetic data, including deformation due to SSEs.

Given that transient SSEs produce permanent offsets in displacement time series observed at the surface, one way to detect them is to use data-driven methods, searching for steps in geodetic time series. Nishimura (2014) scanned moving windows of GNSS time series in Nankai and fitted each segment either with a linear trend or with a linear trend plus an offset associated with potential SSEs. The preferred model was then selected using the Akaike Information Criterion (AIC, Akaike (1974)), allowing a statistical evaluation of the robustness of the models.

Principal Component Analysis (PCA) is also commonly used to separate distinct deformation sources within geodetic data. It assumes that the different physical processes contributing to the signal are orthogonal and can therefore be separated into a small number of dominant eigenmodes. This method has been widely applied to geodetic time series to highlight tectonic transients superimposed on long-term trends or seasonal components (e.g. Kositsky & Avouac, 2010).

Other decompositions are based on Singular Spectrum Analysis (SSA) and its multichannel extension (M-SSA). These techniques decompose time series into periodic signals, trend, and noise components while accounting for temporal correlations, making them particularly suited to extract repeating processes such as seasonal signals. Their ability to recover smooth transient signals from InSAR time series has been demonstrated in various contexts. For instance, Jasir et al. (2024) used SSA to isolate the post-seismic deformation of the 2019 M_w 6 Mirpur earthquake, while Walwer et al. (2025) applied M-SSA to identify volcanic deformation transients at Pacaya volcano.

A more flexible decomposition is provided by Independent Component Analysis (ICA) and its probabilistic variants such as variational Bayesian ICA (vbICA, Gualandi et al., 2016). Unlike PCA, ICA aims to separate statistically independent, non-Gaussian sources, making it particularly effective when deformation processes are not orthogonal. Maubant et al. (2020) used ICA on InSAR time series to extract the transient signal associated with the 2017–2018 Guerrero SSE in the Mexico subduction zone. Similarly, Gualandi and Liu (2021) showed that vbICA can robustly separate tectonic loading from seasonal hydrological deformation in InSAR time series in the San Joaquin Valley and the central San Andreas Fault.

Finally, sparse-representation methods assume that transient deformation can be captured by a sparse set of basis functions. The approach of Riel et al. (2014), based on sparse B-spline coefficients, automatically identified repeating SSEs of varying duration in GNSS time series along the Cascadian subduction zone.

A second group of methods used to detect and extract transient deformation within geodetic data is based on physical models of SSEs. The network inversion filter, proposed by Segall and Matthews (1997), models GNSS displacement time series as a combination of secular velocities, fault slip, benchmark motions, reference frame errors, and estimation errors. It uses a Kalman filter to provide a stochastic description of these components over time, allowing for the separation of transient slip signals from background noise. It provides a kinematic modeling of large SSEs. By adapting the method to InSAR data, Bekaert et al. (2016) analyzed the 2006 SSE in Guerrero, Mexico.

Another approach specifically designed to detect and characterize small-amplitude SSEs is based on correlations between synthetic dislocation-based time series and continuous GNSS data (Rousset et al., 2017). Using a network-based method, it allows the extraction of coherent slow slip surface deformation patterns and provides estimates of the main SSE parameters. The first application was on the Mexican subduction zone (Rousset et al., 2017), and subsequent applications have been performed in various tectonic contexts, including the San Andreas Fault (Rousset et al., 2019), the Nankai subduction zone (Okada et al., 2022), the northern Japan subduction zone (Marill et al., 2024), the South-Central Alaska subduction zone (Okada & Nishimura, 2023), and the southern Peru–northern Chile subduction zone (Jara et al., 2024).

More recently, deep learning approaches have been applied to denoise geodetic time series to better highlight transient deformation signals (Rouet-Leduc et al., 2021; Costantino et al., 2024). These models are trained on synthetic time series that include realistic noise and SSEs and are then applied to different tectonic contexts. Rouet-Leduc et al. (2021) applied such a method to the Ismetpasa segment of the North Anatolian Fault (NAF) in Türkiye, which allowed the extraction of surface deformation due to a known SSE affecting in 2013 (Rousset et al., 2016). Similarly, Costantino et al. (2024) applied this approach to GNSS time series and recovered denoised signals highlighting transient deformation potentially associated with low-amplitude SSEs.

In this study, we adapt the geodetic matched filter, originally developed for GNSS observations (Rousset et al., 2017), for application to InSAR observations in the context of strike-slip faults. Indeed, this method takes advantage of the redundancy of information collected at multiple locations to reduce the detection threshold for low-amplitude SSEs. Given the high spatial density of InSAR observations, it therefore has the potential to detect low-amplitude events compared to the noise amplitude. First, we consider relative displacement time series between pixels located on either side of the fault to mitigate large-scale atmospheric propagation delays. Second, we analyze the noise characteristics of the InSAR time series to construct synthetic time series with realistic noise, which allows us to assess the limitations of our method and to estimate correlation coefficient thresholds for the detection of potential SSEs. Third, following detection, we characterize the main features of the identified SSEs, including their duration and magnitude. Finally, we apply this method to two creeping segments of the NAF, where such events have been documented in previous studies.

2 Method

The geodetic matched filter approach developed by Rousset et al. (2017) is based on physics-based template matching. It enables the detection of SSEs on fault zones by analyzing correlation coefficients between time series of surface displacements derived from geodetic data and templates, corresponding to synthetic dislocation models of SSEs.

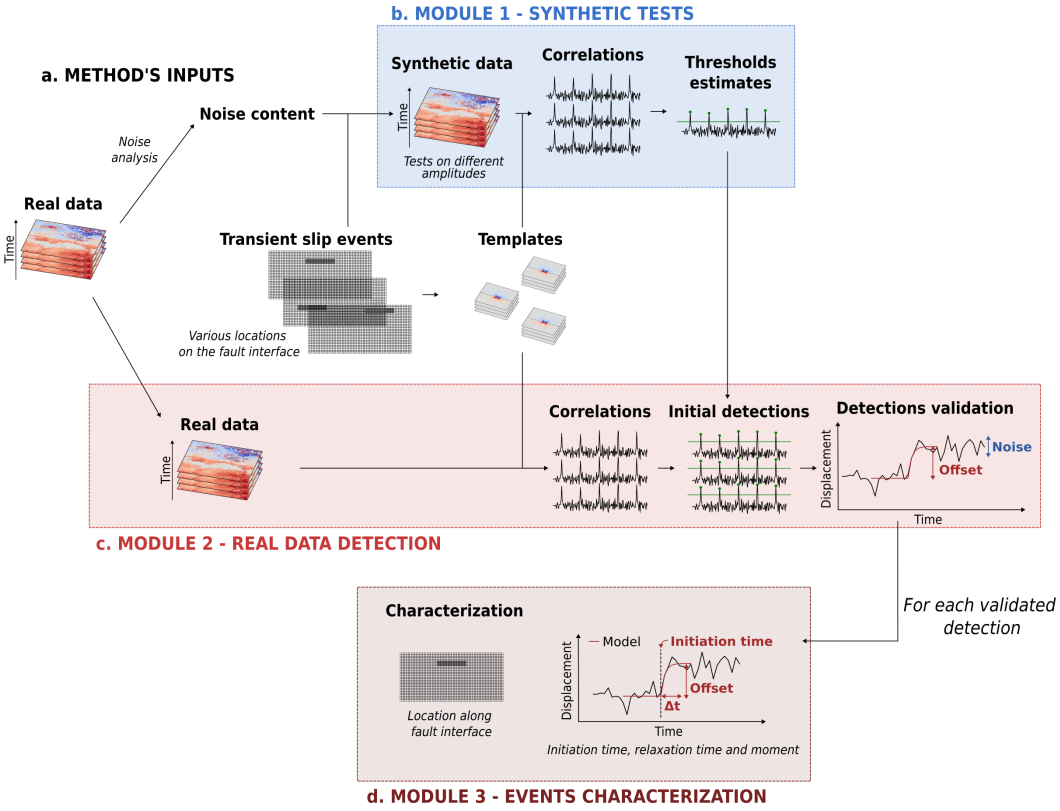

Figure 1. Flow chart presenting the main steps of the method. (a) Method's inputs including analysis of the InSAR noise and construction of the templates. (b) *Module 1*: analysis on synthetic data to determine detection thresholds for SSE identification. (c) *Module 2*: Processing workflow applied to real data, including initial detections and validations. (d) *Module 3*: estimation of the main characteristics of the detected SSEs from real data.

The main phases of the approach presented in Figure 1 are: (a) the preparation of the inputs of the method, (b) the analysis of synthetic time series including realistic noise and synthetic SSEs to estimate detection thresholds, (c) the application to real data to detect potential SSEs with a detections validation step, and (d) the characterization of the SSEs in terms of initiation time and slip amplitude on the fault interface.

2.1 Method's inputs

In this section, we explain the preliminary steps of the method shown in the Figure 1a, leading to the preparation of the method's inputs.

2.1.1 Analysis of realistic noise

To build synthetic displacement time series allowing for thresholds estimates before, we need to analyze the noise content present within the real InSAR displacement time series (Figure 1a). We made the analysis on Line Of Sight (LOS) and East-West (EW) displacement time series, in order to estimate the impact of the noise level on the detectability of the method and evaluate the benefits of post-processing methods.

We assume that the InSAR noise is spatially correlated but temporally uncorrelated, as atmospheric dynamics typically evolve much faster than the revisit period of

Sentinel-1 acquisitions. Spatially correlated noise is generated by filtering white Gaussian noise in the Fourier domain so that its power spectrum follows a negative power-law. Three parameters are estimated from noise extracted from real InSAR time series: (1) the slope of the power spectrum, (2) the mean noise amplitude, and (3) its standard deviation. The slope of the power spectrum is estimated by fitting a linear function in log-log space, which characterizes the spatial correlation of the noise. The mean and standard deviation of the noise amplitude observed in real data are then used to define parameter distributions, ensuring that the synthetic noise reproduces the dispersion within the synthetic data. Histograms representing the distributions of each parameter derived from the real data are shown in supplementary materials (Figures S1 and S2).

2.1.2 Definition of a template

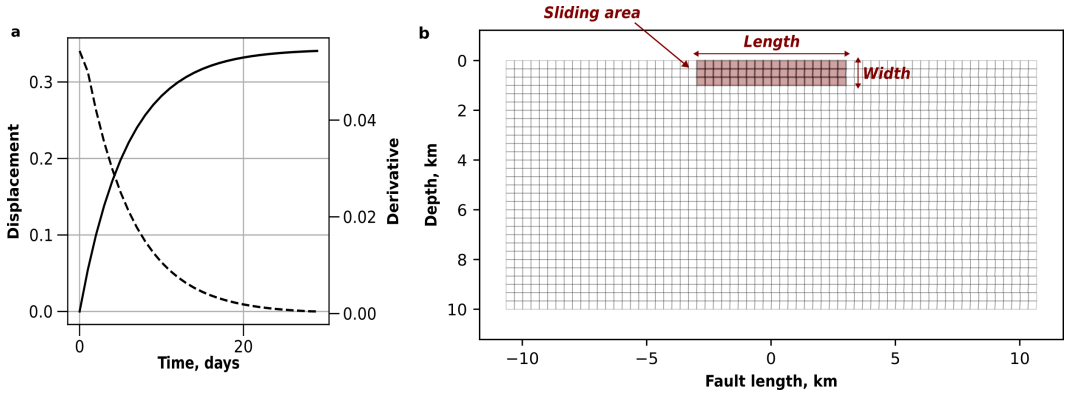

Figure 2. Synthetic template corresponding to surface displacements induced by a sliding area on the fault interface. (a) Relative time series (solid line) of the template computed for the pair of pixels shown in Figure 3a, assuming a relaxation time of 6 *days*. The dotted line corresponds to its temporal derivative. (b) Mesh of the fault interface, with the sliding patches used to build the template shown in red. The fault is meshed with patches of 0.33 $km \times 0.33\ km$, from the surface down to 10 km.

The temporal source function s of synthetic SSEs is defined based on creepmeter measurements on the Izmit segment (Figure S3):

$$s(t_1) = m(1 - e^{-\frac{t_1}{\tau}}) \tag{1}$$

with s the cumulative slip, m the slip amplitude, t_1 the time and τ the relaxation time. The duration of events is estimated by 5τ. The template displacement time series w^i is then obtained by using the following equation:

$$w^i(t_1) = w_s^i.s(t_1) \tag{2}$$

with w_s^i the surface displacement at pixel i deduced from static Green's functions.

An example of a template time series and its temporal derivative is shown in Figure 2a. To reduce spurious detections associated with short-lived spikes, the template displacement time series defined in equation 2 is extended by adding two constant plateaus before and after the transient signal. Each plateau corresponds to a constant value with a duration comparable to that of the transient event. Green's functions, relating slip on a given fault patch to surface displacement, are computed assuming a multi-layered elastic half-space (Zhu & Rivera, 2002), using local velocity and density models for the Izmit and the Ismetpasa segments (detailed in Figure S4, Özalaybey et al. (2011); Laske et al.

(2013); Rousset et al. (2016); Karabulut (2025)). An example of the mesh of the fault interface is shown in Figure 2b.

2.2 Module 1: Detection of synthetic slow slip events

The following parts explain the steps of the *Module* 1 shown in the Figure 1b, leading to the analysis on synthetic displacement time series.

2.2.1 Building the synthetic data

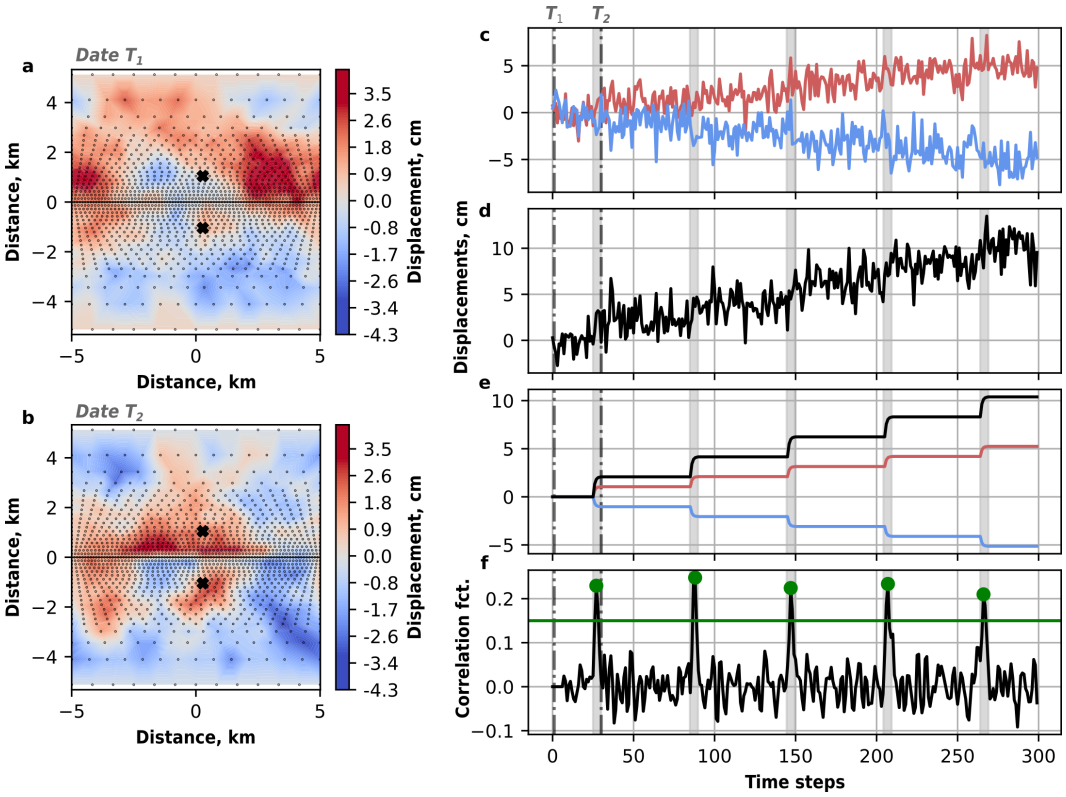

Figure 3. Examples of synthetic InSAR time series and correlation functions. (a,b) Synthetic cumulative surface displacement fields including (a) only realistic synthetic noise at a date T_1 and (b) realistic noise and a SSE located in the middle of the fault trace (shown in black) at a date T_2. SSEs are built using a sliding patch of 6 km-length and 1 km-width, centered at a depth of 0.67 km, with a magnitude of 4.55. Black dots indicate pixel locations after decimation. (c) Synthetic time series for the two pixels marked by black crosses in panels (a, b), located on either side of the fault. The blue curve corresponds to the northern pixel and the red curve to the southern pixel. (d) Relative time series obtained by differencing the two time series shown in (c). (e) Synthetic SSE templates inserted into the time series, for the two pixels and for their relative time series. (f) Correlation functions associated with the sliding patch used to build the synthetic SSEs. The green line and dots show the detection threshold and the detected peaks, respectively. (c-f) Thick gray vertical lines correspond to the occurrence and duration of the synthetic SSEs added to the time series. Vertical dash-dotted lines indicate the two dates used to plot the maps (a,b).

We use the real InSAR noise characteristics (Section 2.1.1) to build synthetic displacement time series cubes. To sample the full range of parameter combinations according to their associated probabilities in the synthetic time series, parameters are randomly drawn from these empirical distributions. To mitigate residual atmospheric signals present within InSAR displacement time series, we decided to use relative displacement time series between all pairs of pixels located on either side of the fault. It has the advantage to remove similar amplitudes of the residuals at nearby pixels and to enhance the tectonic signal by taking pixels on either side of the fault. The relative surface displacement between the pair of pixels i and j noted $w^{i,j}$ is estimated by:

$$w^{i,j}(t_1) = w^i(t_1) - w^j(t_1) \tag{3}$$

The final synthetic displacement time series cubes are constructed by combining realistic noise with one or several synthetic SSEs using equation 3. Examples of synthetic time series are presented in Figure 3 – a,b,c,d, with panel 3d showing the relative displacement time series (in black) between two displacement time series from a pair of pixels on either side of the fault (panel 3c).

We also decimate the initial pixels using an exponential relationship with the distance from the fault for the Izmit segment and a quadratic one for Ismetpasa (smaller study area), to decrease the number of pixels, as shown by the black dots in Figure 3 – a,b. We will show the influence of decimation on our results in the next part (see section 2.2.2).

2.2.2 Correlation functions

The correlation functions $C^{i,j}$ used to detect the SSEs are computed between the template relative displacement time series $w^{i,j}$ and the InSAR relative displacement time series $d^{i,j}$ of each pair of two pixels i and j located on either side of the fault. As described by Rousset et al. (2017), we use the temporal derivative of $w^{i,j}$ (Figure 2a) and $d^{i,j}$ so that:

$$C^{i,j}(t) = \frac{< \dot{w^{i,j}}(t_1), \dot{d^{i,j}}(t_2) >_{N,\Delta t}}{\sqrt{< \dot{w^{i,j}}(t_1), \dot{w^{i,j}}(t_1) >_{N,\Delta t} < \dot{d^{i,j}}(t_2), \dot{d^{i,j}}(t_2) >_{N,\Delta t}}} \tag{4}$$

with N the number of time steps of the template ($N = ||t_1|| = ||t_2||$) and Δt the temporal sampling. $< w^{i,j}(t_1), d^{i,j}(t_2) >_{N,\Delta t}$ the inner product is defined as:

$$< w^{i,j}(t_1), d^{i,j}(t_2) >_{N,\Delta t} = \sum_{k=0}^{N-1} w^{i,j}(t_1 + k\Delta t) d^{i,j}(t_2 + k\Delta t). \tag{5}$$

The correlation is then weighted by the amplitude of the Green's function at each pair of pixels (i, j):

$$C_w^{i,j}(t) = (|w_s^i|.|w_s^j|) C^{i,j}(t). \tag{6}$$

A more important weight is given to pixels that are supposed to be the most affected by the SSE.

Finally, the correlation coefficients used for SSE detections are the mean average of all $C_w^{i,j}$ computed for every pair of pixels (i, j). An example of correlation coefficients are shown in Figure 3f.

Comparison of the maximum values of the correlation functions estimated for the same displacement time series cube one shallow slow slip event (SSE) (depth 500 m – M_w 4.8) and a realistic InSAR noise but applying different decimation ratios shows that the correlation values are similar ($\pm$ 0.035), however it enables to significantly reduce the computation time by $\sim$ 96% (see Figure S5).

2.2.3 Thresholds estimates

The occurrence of potential SSEs in the data is highlighted by high values of the correlation coefficients, relative to a given threshold. An example is shown in green in Figure 3f. To estimate the optimal thresholds and to analyze the sensitivity of the method, we first use synthetic displacement time series built in the previous section (Section 2.2.1). We use a synthetic displacement time series cube composed of 100 events over a period of 6000 time steps. Each synthetic SSE has a slip area of ~ 6 km in length and ~ 1 km in width, with a relaxation time of ~ 6 $days$. These parameters have been calibrated according to the characteristics of observed shallow SSEs reported in previous studies (Rousset et al., 2016; Neyrinck et al., 2024; Özdemir et al., 2025). The influence of both the template area and the relaxation time on the correlation functions is analyzed in the supplementary materials: a template length that is twice as long or twice as short as the real SSE length decreases the correlation coefficient by ~ 2 (Figure S6); a relaxation time that is too long will both decrease the correlation coefficient and shift the detection in time (Figure S7).

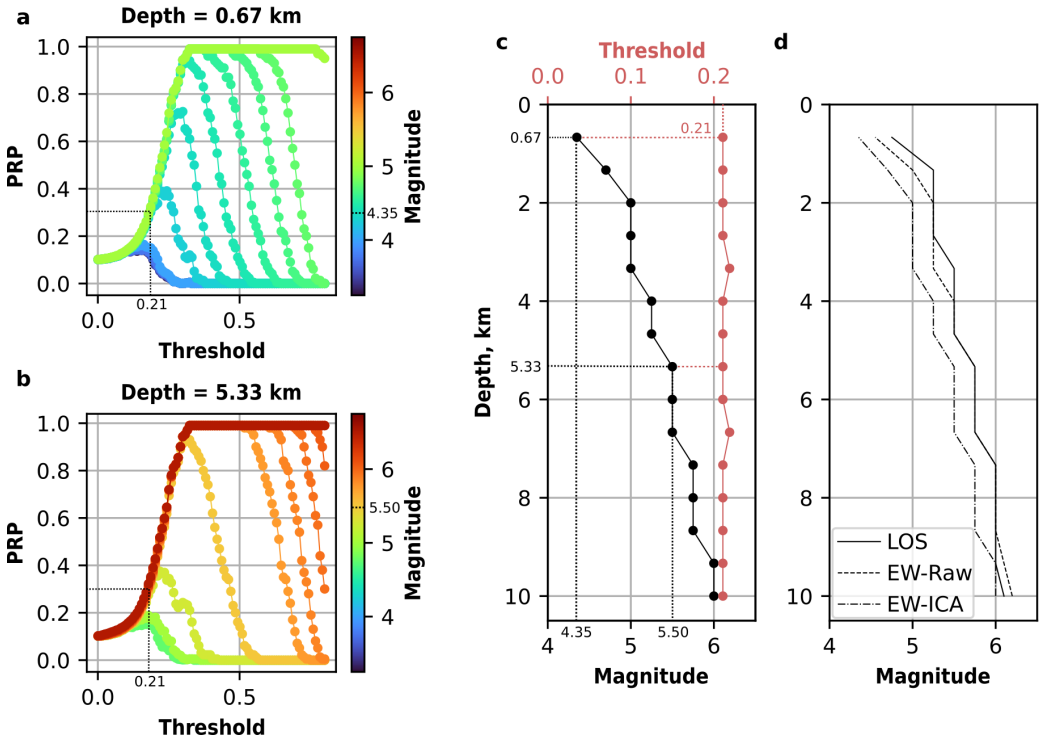

Figure 4. Precision-recall products (PRP) estimated for various synthetic SSE depths and event magnitudes, compared to the thresholds used for the detection. (a,b) PRP obtained for events at depths of 0.67 km (a) and 5.33 km (b). Each colored line corresponds to a given magnitude. (c) Minimum detectable magnitudes (black) and associated thresholds (pink) for $PRP \geq 0.4$ as a function of depth. The dotted lines show the selected minimum magnitude and threshold corresponding to $PRP \geq 0.4$ at both depths shown on panels (a,b). (d) Comparison of the minimum magnitudes estimated using synthetic noise from three different datasets: LOS (solid line), EW-Raw (dotted line) and EW-ICA (dash-dotted line).

To analyze the reliability of the detections on synthetic displacement time series, we compute the precision-recall product PRP, defined as:

$$PRP = \frac{TP}{AP}.\frac{TP}{RP}, \tag{7}$$

with TP corresponding to the true positive detections (i.e. the number of detections corresponding to synthetic SSEs added to the displacement time series), RP the real positive detections (i.e. the initial number of SSEs in the synthetic displacement time series) and AP all the positive detections (i.e. true and false positive detections). PRP lies between 0 and 1, with $PRP = 1$ indicating that all the SSEs in the synthetic displacement time series are detected, with no false detection. The first ratio TP/AP estimates the fraction of true detections (i.e. the precision), while the second ratio TP/RP estimates the number of detected events relative to the number of events in the time series (i.e. the recall). This product is estimated by combining all the detections associated with the ensemble of fault patches along the fault interface. Figure 4 – a,b shows PRP as a function of the selected threshold for two given depths of the synthetic SSEs. By using this precision-recall product, we can estimate the minimum magnitude of the events that can be detected by this method as a function of the depth of the synthetic SSEs, and the corresponding threshold for a given $PRP \geq p$, with p representing the confidence of the detections. The final results for this synthetic displacement time series with $PRP \geq 0.4$ are shown in Figure 4c. By applying these thresholds to the correlation functions, we detect potential SSEs.

2.3 Module 2: Real data peak detection

The following parts explain the steps of the *Module* 2 shown in the Figure 1c, leading to the detection of SSEs with the real InSAR displacement time series. Some parts have already been explained in the previous section (Section 2.2).

2.3.1 Validation of the detections

In order to detect small magnitudes SSEs, we need to choose a relatively low PRP to decrease the minimum magnitudes of SSEs detectable using this approach (Figure 4c) and according to the InSAR noise present in the data (Figure 4d – test of three different types of noise). Therefore, we define two conditions tested beforehand using synthetic displacement time series, that allow us to select the detections obtained from the correlation functions, and remove false detections due to the choice of a low PRP.

The first condition is based on the number of neighboring sliding patches triggering a positive detection. Due to the difference between the synthetic SSE sliding patch size and the discretizations of the fault interface (areas of 0.33 x 0.33 km^2), a SSE must be detected on several neighboring sliding patches in the horizontal direction. We therefore discard detections associated with a single horizontal sliding patch.

The other condition is based on a weighted stack of displacement time series at each pixel centered on the detection time. The aim of the stack is to enhance the signal-to-noise ratio by stacking the raw displacement time series, weighted by the Green's functions w_s^i associated with the template that exhibits the maximum correlation coefficient. An example of a synthetic stacked time series is shown in Figure 5. The offset associated with the SSE is related to the source slip and the slipping area. To validate the detection, we compute the offset by taking the difference between the averages over $6 - months$ time windows before and after the detection. We validate the detection if this offset is larger than the standard deviation of the stacked time series computed on a period of 5 *months* centered on the detection.

Figure 6 – a,b shows the effect of the validation for two synthetic displacement time series including SSEs at two distinct depths, with $PRP \geq 0.4$. It shows that the val-

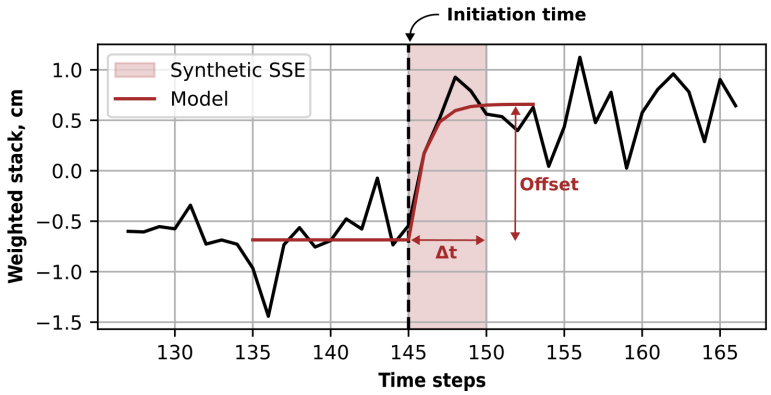

Figure 5. Example of a weighted stack (black line) of synthetic displacement time series including an SSE of M_w 4.65, located at 0.67 km-depth. The red rectangle shows the duration of the synthetic SSE. The red curve corresponds to the model obtained during the characterization step, allowing the estimate of the initiation time (dotted line), offset and relaxation time (related to the duration Δt).

idation step allows to separate well true positive detections from true negative ones. Some false positive detections remain, usually corresponding to low offset amplitudes.

Figure 6d shows TP/RP and TP/AP ratios before and after the validation step, obtained with different initial PRP values for synthetic SSEs located at 0.67 km-depth (Figure S8 presents a similar figure for the Ismetpasa configuration). The TP/AP ratio (in green) is significantly improved by the validation step for low PRP. We also observe a decrease in the TP/RP ratio (in blue), which is important for $PRP = 0.1$ and of approximately ~ 0.1 for larger PRP. This can be explained by the fact that for low PRP, the tested magnitudes are lower (as shown by panel 6c), leading to SSE offsets that are close to the noise level.

In order to maximize the probability of capturing SSEs while maintaining a confidence of getting true positive detections larger than 0.9, we chose an initial $PRP \geq 0.4$ for the real InSAR data, corresponding to $TP/RP \geq 90\%$ at the minimum detectable magnitude. The validation step makes it possible to choose a lower PRP while keeping a high probability of detecting true events, and thus further reduce the minimum detectable magnitude.

2.4 Module 3: Characterization of the events

The following section explains the steps of the *Module 3* shown in Figure 1d. After the validation of the detections, we estimate several characteristics of the detected SSEs, including their location along the fault and at depth, the initiation time, the relaxation time and the equivalent magnitude of the event.

2.4.1 Location of the events

For the Izmit segment, the spatial extent of the sliding patch is fixed to 6 km-length by 1 km-width, based on previous studies properly extracting slip area (Neyrinck et al., 2024). The along-fault and depth locations for a given location correspond to the patch with maximum correlation amplitude. The Figure S9 shows the impact of the chosen size of the sliding patch on the final magnitude estimates of the events by comparing the estimated moments with the inital ones, for different sizes and different magnitudes. By

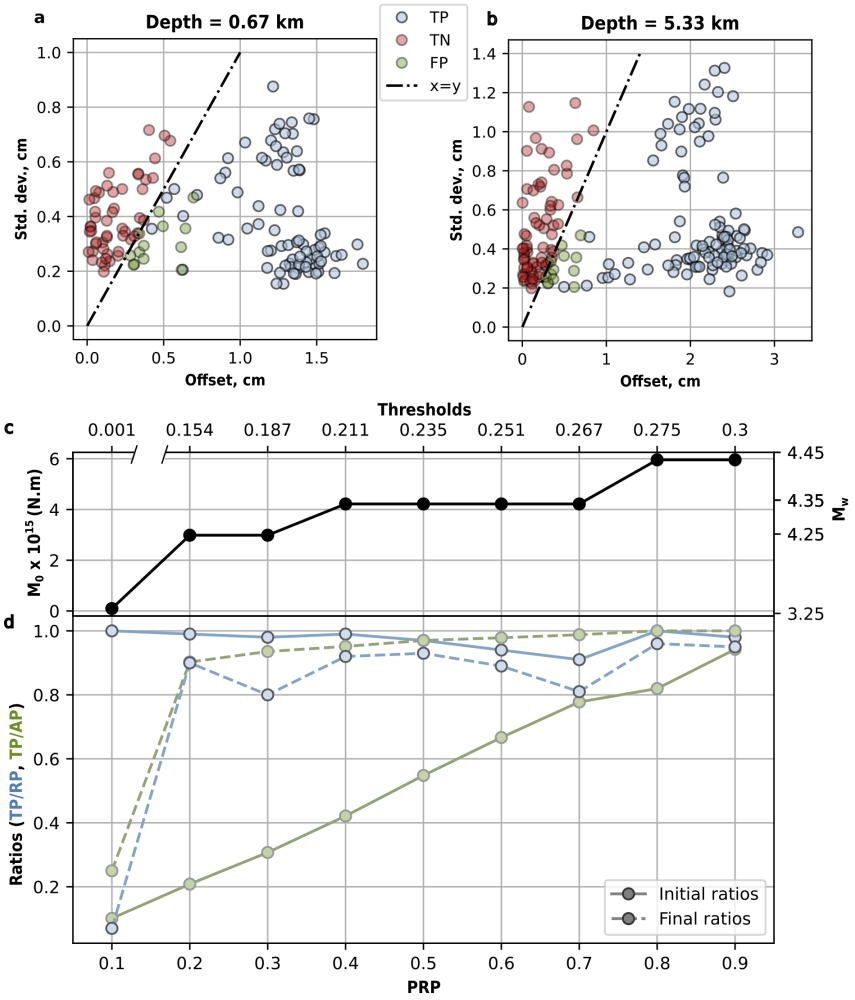

Figure 6. Final detections of synthetic SSEs after the validation step. (a,b) Comparison between the estimated offsets and the standard deviation of the weighted stacks for each detection for synthetic SSEs at a depth (a) of 0.67 km and (b) of 5.33 km. TP, TN, and FP denote true positives, true negatives and false positives, respectively. The dash-dotted line indicates the threshold where the offset equals the standard deviation, which is used to separate positive from negative detections. (c) Minimum moments M_0 (and corresponding magnitudes M_w) detected as a function of PRP and estimated before the validation step. (d) TP/RP and TP/AP ratios as a function of PRP, shown in blue and green, respectively. Solid and dotted lines correspond to the ratios before and after the validation step, respectively. Panels (c) and (d) correspond to synthetic SSEs at a depth of 0.67 km.

using a smaller patch, we tend to underestimate the magnitude, whereas a larger patch overestimates it. However, even by using the smaller patch, the magnitude estimate error is up to ~ 0.17. The accuracy of the location along the fault and at depth estimates of the sliding patch is shown in Figure S10 – a,b, at a function of depth and PRP. High PRP improves the estimate accuracies, and we see a decrease of the depth estimate accuracy for deeper sliding patches due to a larger spatial extent of the related surface deformation reaching the edges of the study area.

2.4.2 Initiation time and relaxation time

As for the validation step of the detection (section 2.3.1), we use the stacked displacement time series weighted by the Green's functions coefficients w_s^i associated with the patch of larger correlation coefficient (Rousset et al., 2017). The stacked time series is then fitted by the temporal function used to describe the template time evolution (equation 2) and is set to zero beforehand. The initiation time and relaxation time are estimated by minimizing the root-mean-square error (RMSE) between the model and the weighted stacked time series. An example of the best model is shown in Figure 5. The RMSE calculation is weighted, with more weight at the center of the time series, to emphasize the transient signal. The accuracy of the relaxation time and initiation time estimates based on synthetic tests are presented in Figure S10 – c,d as a function of depth for 3 values of PRP. The relaxation time is overestimated by ~ 6 $days$, due to the low InSAR return time, which is comparable with the relaxation times of SSEs. However, the initiation time is well resolved, with an error of ± 5 $days$, consistent with the return time of the InSAR data obtained from Sentinel-1 images.

2.4.3 Magnitude

By using the offset surface displacement of the modeled SSE to compute the temporal parameter, and the fixed template slip dimensions of the sliding patch, we compute the moment M_0 and the associated moment magnitude M_w using the following equations:

$$M_0 = \mu.S.\Delta u, \tag{8}$$

$$M_w = \frac{2}{3}.(log_{10}M_0 - 9.1), \tag{9}$$

with μ the shear modulus, S the slipping surface and Δu the slip amplitude. The accuracy of magnitude estimate from synthetic tests shows that the magnitude is well recovered for sliding patches down to a depth of 5 km and is slightly overestimated at greater depths (Figure S10e).

3 Application to the North Anatolian Fault

3.1 Tectonic context and InSAR data processing

The NAF is a major continental right-lateral strike-slip fault system accommodating the westward extrusion of Anatolia relative to Eurasia (Şengör et al., 2005). Two segments are characterized by shallow aseismic creep and episodic SSEs, documented using creepmeters, GNSS, and InSAR observations (Ambraseys, 1970; Cakir et al., 2005; Çakir et al., 2012; Bilham et al., 2016; Rousset et al., 2016; Jolivet et al., 2023; Neyrinck et al., 2024).

In this study, we apply the geodetic matched filter approach to the two creeping segments: the Izmit segment (Figures S11a and S12a), which ruptured during the 1999 M_w 7.6 earthquake (Barka, 1999), and the Ismetpasa segment (Figures S11b and S12b), which ruptured during the 1944 M_w 7.3 earthquake (Stein et al., 1997). Both segments have hosted multiple shallow SSEs since their last major ruptures (Aslan et al., 2019; Neyrinck et al., 2024; Özdemir et al., 2025), providing independent constraints for validation of our detections. Because of their strike direction close to 90°, the locations along the fault is also expressed in the following parts by the longitudes.

The InSAR displacement time series are automatically processed within the FLATSIM framework (Thollard et al., 2021), using a Small Baseline Subset approach (NSBAS, Doin et al., 2011). In order to assess the influence of noise reduction and signal extraction on SSE detectability, we consider several levels of post-processing. These include raw Line-Of-Sight (LOS) displacement time series, East-West (EW) displacement time

series obtained after geometric decomposition and seasonal signal removal, and further post-processed EW displacement time series in which non-tectonic components are isolated and removed using Independent Component Analysis (ICA).

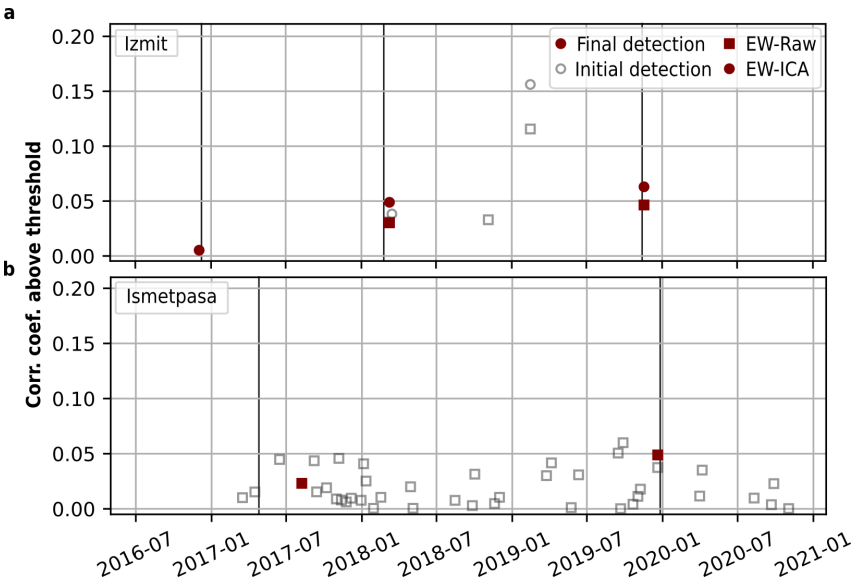

Figure 7. Final peak detection obtained for the Izmit segment (a) and the Ismetpasa segment (b). The peaks are shown by their difference between the correlation coefficients and the thresholds. Filled red circles highlight final validated detections (after the validation step – Section 2.3.1), whereas empty gray circles are considered as false detections. Two datasets from different post-processing sequences are considered: the EW-Raw (squares) and EW-ICA (circles) datasets (cf. the description of the datasets in part 3.2; the LOS dataset resulting in zero detection is therefore not shown here). The vertical lines correspond to initiation times of SSEs recorded along both segments by creepmeters (Figures S12, S15 and S16).

3.2 Application to the Izmit segment: influence of InSAR post-processing

We first apply the method to the Izmit segment to investigate how InSAR post-processing affects SSE detection performance. Three datasets are tested: (1) raw LOS displacement time series from Sentinel-1 ascending track *A*058, (2) EW displacement time series after horizontal-vertical decomposition and removal of seasonal signals (EW-Raw), and (3) EW displacement time series further denoised using ICA (EW-ICA). The detailed post-processing method used for the datasets (2) and (3) is described by Neyrinck et al. (2024), consisting in a seasonal and linear decomposition of the signal to remove the non-tectonic annual periodic terms, a horizontal-vertical decomposition of the LOS displacement time series using ascending and descending tracks (producing the EW-Raw dataset) and the application of an Independent Component Analysis (ICA) on the pixels of the previous EW-Raw displacement time series within the sedimentary basin (producing the EW-ICA dataset).

Based on the synthetic tests presented in Section 2, we adopt an initial precision-recall product of $PRP \geq 0.4$ for the Izmit segment. The minimum detectable magnitudes inferred from the synthetic experiments (Figure 4d) indicate that LOS and EW-Raw datasets yield comparable detection thresholds, with slightly improved sensitivity at shallow depths for the EW-Raw case. In contrast, the EW-ICA dataset consistently

Table 1. Results of the characterization of the five SSEs detected using the geodetic matched filter approach along the Izmit and Ismetpasa segments, compared to previous works. IZ and IS stand for Izmit and Ismetpasa, and Cm. stands for Creepmeters. The references are the following ones: [1] for Aslan et al. (2019), [2] Jolivet et al. (2023), [3] Neyrinck et al. (2024) and [4] Özdemir et al. (2025). $*$ indicates results from this study, and $-$ indicates that no information is available for this feature.

Seg.	**Initiation time**	**Lon.** (°)	**Depth** (km)	**Relaxation time** ($days$)	**Duration** ($days$)	M_w	**Ref.**
IZ	30/11/2016	-	-	-	-	-	Cm.
	$-$/12/2016	29.98	-	-	21	-	[1]
	$-$/12/2016	29.85	-	-	-	-	[3]
	03/12/2016	30.025	1.00	1.0		4.16	$*$
IZ	$-$/03/2018	30.03	0.5	-	21	4.4	[3]
	10/03/2018	30.038	1.00	6.4		4.29	$*$
IZ	25$-$29/11/2019	-	-	$1.4-3$	9	-	Cm.
	$-$/11/2019	30.04	1.00	-	21	4.3	[3]
	18/11/2019	30.05	1.00	5.1	-	4.29	$*$
IS	11/06/2017	-	-	9.7	-	-	Cm.
	mid 2017	32.62	-	-	-	-	[2]
	08/08/2017	32.58	2.10	2.8	-	4.41	$*$
IS	21/12/2019	-	-	9.3	-	-	Cm.
	late 2019	32.62	-	-	-	-	[2]
	21/12/2019	32.65	< 2	-	26	4.8	[4]
	20/12/2019	32.61	0.43	11.9	-	3.98	$*$

allows the detection of lower–magnitude events at all depths, highlighting the benefit of advanced noise reduction.

When applying the matched filter to the real data (Figure 7a), no SSE is detected using the LOS dataset, indicating that residual atmospheric and non-tectonic signals dominate the displacement time series at this processing level. Using the EW-Raw dataset, two SSEs are detected in 2018 and 2019. The EW-ICA dataset enables the detection of an additional event in 2016 and yields systematically higher correlation coefficients for all detected events, demonstrating an improved signal-to-noise ratio. The three events detected are consistent with the three event already documented in published articles (Aslan et al., 2019; Neyrinck et al., 2024).

The detected events are subsequently characterized following the procedure described in Section 2.4. Figure 8 illustrates the characterization of the 2019 event. The highest correlation coefficients correspond to a sliding patch centered at approximately $30.05°E$ and at about 1 km depth, within the Izmit sedimentary basin (Özalaybey et al., 2011). The corresponding weighted stack displacement time series (Figure 8b) exhibits a clear transient offset that is well fitted by the adopted temporal source function. Independent creepmeter records from the Izmit-Seller and Tepetarla sites show contemporaneous transient displacements (Figure 8c), providing an external validation of the InSAR-based detection. Similar figures for the characterization of other detections using EW-Raw and EW-ICA datasets are shown in Figure S13.

For the three events detected using the EW-ICA dataset, the estimated magnitudes range between M_w 4.1 and M_w 4.35, with relaxation times between ~ 1 and 5.3 $days$, all estimates being gathered in Table 1. Previous InSAR and creepmeters analyses of SSEs along the Izmit segment already provided some estimates, and are also gathered in Ta-

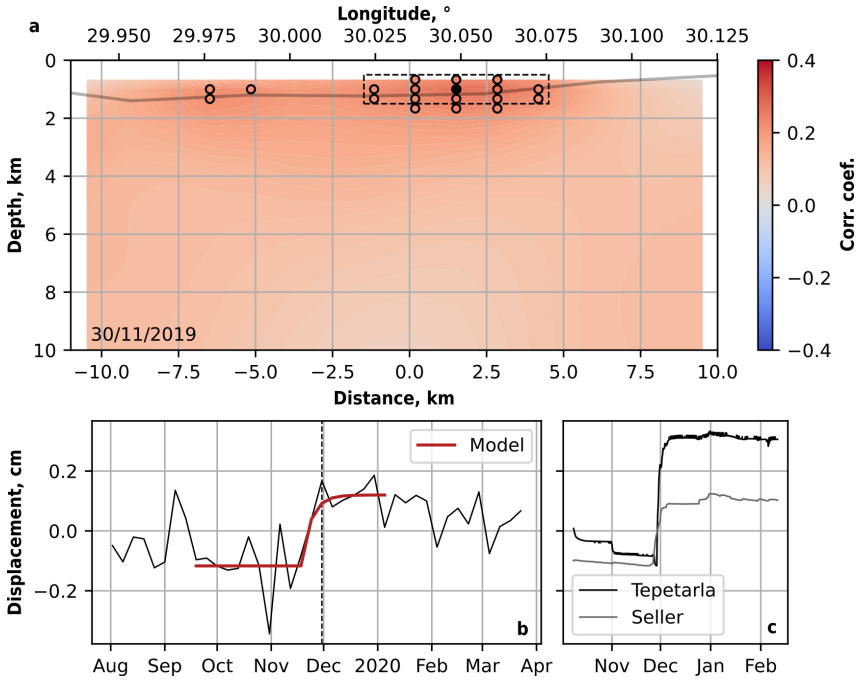

Figure 8. Example of the 2019 SSE detected along the Izmit segment (Figure 7a). (a) Correlation coefficients along the fault interface at the date of the detection for the EW-ICA dataset. Dots indicate spatial detections, with the black one marking the patch with the highest amplitude, corresponding to the center of the template (dotted black line). The gray line shows the downdip boundary of the sedimentary basin (Özalaybey et al., 2011). (b) Weighted stack displacement time series for the template highlighted in (a) by the dotted black line. The best fitting model is shown in red. The vertical dotted line shows the time of highest correlation amplitude. (c) Creepmeter records in Izmit-Seller and Tepetarla sites, showing cumulative displacement over the same period. The locations of both creepmeters are shown in Figures S11a and S12a (Bilham et al., 2016; Emre et al., 2018).

ble 1. We observe a good consistency with the creepmeters data of the initiation time with $\Delta t_0 \approx 4{-}11$ *days*. The duration or relaxation time obtained by the geodetic matched filter approach leads to higher values for the 2018 and 2019 SSEs, whereas the estimates corresponding to the 2016 event is much lower, probably due to the variations of the signal-to-noise ratios between the three weighted stack displacement time series (Figure S13). A comparison of the tectonics (Figure 8 – b,c) for the 2019 event shows smaller duration of the event according to the creepmeters data. The inferred sliding patches are shallow (≤ 2 *km* depth) and display a slight eastward migration with time, consistent with previous InSAR analyses of SSEs along the Izmit segment (Aslan et al., 2019; Neyrinck et al., 2024).

3.3 Application to the Ismetpasa segment

We next apply the geodetic matched filter approach to the Ismetpasa segment in order to test its robustness in a different location along the NAF with a distinct noise environment. For this segment, we use the EW-Raw dataset only, ICA attempts being unsuccessful on that segment. The noise characteristics are recomputed locally (Figure S2) to derive segment-specific detection thresholds (Figure S8). Due to the higher noise level, a lower precision-recall product ($PRP \approx 0.2$) is adopted. Based on previous geodetic

observations and inverse slip models (Rousset et al., 2016), we also use a smaller template size (3 km length and 1 km width).

The initial application yields to 55 candidate detections (Figure 7b). After applying the validation criteria based on spatial coherence and weighted stack displacement time series (Section 2.3.1), only two detections remain, occurring in August 2017 and December 2019 (Figure S14).

The retained events have estimated magnitudes between M_w 4.0 and M_w 4.4 and are located at a shallow depth ranging from ~ 0.4 to 2 km (Table 1). The inferred relaxation time ranges between 3 and 12 *days*. Despite larger uncertainties than for the Izmit segment, these estimates are consistent with previous InSAR, GNSS, and creepmeter observations along the Ismetpasa segment (Table S1; Bilham et al., 2016; Jolivet et al., 2023; Özdemir et al., 2025). The first detection in August 2017 seems related to the 2017 SSE recorded along the Ismetpasa segment (Figure 7b), despite a difference of ~ 58 *days* of the intiation time with the creepmeter record (Figure S16). The relaxation time is therefore also lower than observed on the creepmeter data, due to the temporal shift of the detection. The 2019 event is detected with only one-day delay, but large differences of the estimates: a relaxation time difference up to 3 *days* compared to the creepmeters records, and a duration difference up to 30 *days* compared to GNSS data. We also obtain a lower magnitude than the one calculated using the GNSS data.

Overall, the application of our method to the Ismetpasa segment confirms that the geodetic matched filter approach can successfully identify SSEs in independent datasets, even under less favorable noise conditions. The comparison between the Izmit and Ismetpasa segments highlights the importance of local noise characterization and appropriate InSAR post-processing to maximize the sensitivity and reliability of automatic SSE detection.

4 Discussion

4.1 Validation of the approach and assumptions

The results obtained from both synthetic tests and real-data applications demonstrate that the adapted geodetic matched filter approach is capable of detecting and characterizing shallow SSEs using InSAR time series. Synthetic experiments (Figures 4 and 6) show that, for realistic noise conditions, SSEs with a magnitude down to $M_w \sim 4 - 4.5$ can be detected at shallow depths with a confidence level exceeding 90 % after the validation step (Figure 6 – c,d). The minimum detectable magnitude increases with depth, as expected from the decay of surface displacement with increasing source depth (Figure 4c).

The application to the Izmit and Ismetpasa segments further confirms the robustness of the approach. Along the Izmit segment, the three previously documented events (Aslan et al., 2019; Neyrinck et al., 2024) are successfully retrieved when applying the method to the EW-ICA dataset (Figures 7a, 8 and S13), and their estimated magnitudes (M_w 4.1−4.3), depths (≤ 2 km), and relaxation times are consistent with previous InSAR and creepmeter analyses (Aslan et al., 2019; Neyrinck et al., 2024). Along the Ismetpasa segment, two events are detected after validation (Figure 7b and Figure S14), with magnitudes and durations comparable to earlier geodetic observations (Rousset et al., 2016; Özdemir et al., 2025), although with larger uncertainties. The agreement between detected events, weighted stack characterization (Figure 8b), and independent creepmeter records (Figure 8c and Figures S15 and S16) provides an external validation of the method.

A key outcome of this study is the strong dependence of detection capability on the noise level and post-processing strategy. The comparison between LOS, EW-Raw,

and EW-ICA datasets along the Izmit segment (Section 3.2; Figure 4d) shows that post-processing substantially lowers the detection threshold. While no event is detected using raw LOS time series, the EW-Raw dataset enables the recovery of two events, and the EW-ICA dataset allows the detection of an additional, smaller event with systematically higher correlation peaks. These results highlight that the sensitivity of the matched filter is primarily controlled by the signal-to-noise ratio of the input time series.

Despite these encouraging results, several assumptions we made impose limitations. First, the spatial extent of the template used during the SSE characterization (Section 2.4) is fixed. This choice is motivated by the difficulty of resolving source dimensions from InSAR data alone, given the strong spatial covariance of atmospheric noise at kilometer scale ($\leq 5\ km$), which can generate deformation patterns partially mimicking shallow SSE signals. Indeed, the estimated PSD slopes (≈ 2.5–4; Figures S1 and S2) are consistent with atmospheric turbulence and imply a steep power-law spectrum dominated by long wavelengths. Such spectral behavior indicates substantial spatial correlations at scales comparable to the expected dimensions of shallow SSE sources.

Second, the temporal evolution of the template is defined by a fixed relaxation time ($\tau = 6\ days$), calibrated from previous observations along continental strike-slip faults (Rousset et al., 2016; Neyrinck et al., 2024; Özdemir et al., 2025). As shown in Figure S7, using a relaxation time significantly different from that of the real event reduces correlation amplitudes and may shift detection times. The adopted value represents a compromise: it maximizes sensitivity to SSEs with durations of a few weeks while reducing spurious correlations during noise-only periods. However, events with relaxation times substantially different from the assumed template value would produce lower correlation amplitudes and therefore be detected with reduced efficiency.

Third, the method assumes temporally uncorrelated but spatially correlated noise when generating synthetic time series (Section 2.1.1). Although this assumption is justified by the short characteristic timescale of atmospheric variability relative to the Sentinel-1 revisit period, residual temporally correlated signals (e.g., hydrological loading) may still affect detection performance. The improvement observed when applying ICA (Section 3.2) illustrates that incomplete separation of non-tectonic signals directly impacts the minimum detectable magnitude.

Finally, the temporal resolution of InSAR (6 *days* for Sentinel-1A/B) inherently limits the precision of initiation time and relaxation time estimates. Synthetic tests (Figure S10 – c,d) indicate a systematic overestimate of the relaxation time by $\sim 6\ days$, and comparisons with creepmeter records (Section 4.2) show discrepancies of up to one SAR acquisition interval for initiation times. These differences reflect both the coarse temporal sampling of InSAR and the different spatial sensitivities of creepmeters and InSAR observations.

Overall, the combined synthetic validation and successful retrieval of independently documented SSEs demonstrate that the proposed approach provides a reliable and systematic framework for detecting shallow SSEs in the InSAR time series. At the same time, its performance remains conditioned by noise characteristics, template assumptions, and the intrinsic spatial and temporal resolution of the data. These aspects should be carefully considered when applying the method to other tectonic contexts.

4.2 Comparison with independent geodetic observations along the NAF

A detailed comparison with previously published creepmeter, GNSS, and InSAR studies provides an independent assessment of the robustness of the geodetic matched filter approach along the Izmit and Ismetpasa segments of the NAF. We focus here on the consistency of the inferred spatiotemporal parameters and on the origin of remaining discrepancies.

4.2.1 Izmit segment

Along the Izmit segment, the three events retrieved with the EW-ICA dataset correspond to the 2016, 2018, and 2019 SSEs previously documented using InSAR time series and slip inversions (Aslan et al., 2019; Neyrinck et al., 2024). The estimated magnitudes ($M_w \sim 4.1 - 4.3$) and shallow depths ($\leq 2\ km$) are consistent with the slip models inferred by Neyrinck et al. (2024), in which the creeping section is confined within the sedimentary basin (Figures 8a and S13). The spatial location of the sliding patches inferred from the maximum correlation coefficients falls within the areas of significant slip in those models, indicating that the template-based approach captures the first-order geometry of the events without performing a full inversion.

Temporal parameters derived from the weighted stack analysis (Figure 8b and S13) are also comparable to independent creepmeter observations (Figure 8c and Figure S15). The initiation times agree within approximately one to two Sentinel-1 revisit time ($6-12\ days$). Relaxation times estimated from the matched filter approach (e.g., $\sim 5.3\ days$ for the 2019 event) are slightly longer than those inferred from creepmeters ($1.4-3\ days$). This systematic difference likely reflects (i) the coarse temporal resolution of InSAR compared to the $30s$ sampling of creepmeters, and (ii) the fact that creepmeters record slip over a few tens of meters at the surface, whereas InSAR integrates deformation over kilometer-scale fault areas.

4.2.2 Ismetpasa segment

Along the Ismetpasa segment, two events are retained after validation and can be compared with previous InSAR, GNSS, and creepmeter analyses (Jolivet et al., 2023; Özdemir et al., 2025). The 2019 event, characterized by GNSS by Özdemir et al. (2025) with an equivalent magnitude of ~ 4.8 and a duration of $\sim 26\ days$, is also identified by our approach with a shallow depth ($< 2\ km$) and a duration of a few months ($\sim 60\ days$). Although our magnitude estimate is slightly smaller, this discrepancy can be partly attributed to the fixed template size used in the characterization step (Figure S9), which may underestimate the moment if the true slipping area exceeds the prescribed dimensions. As described in Özdemir et al. (2025), the signal-to-noise ratio of the GNSS surface displacements is too low to permit a reliable inversion. We reach a similar conclusion using the InSAR observations.

The mid-2017 event is more weakly constrained. While a correlation peak is identified (Figure 7b), the inferred initiation time differs by up to three months from the N. Wall creepmeter record (Figure S16). An increase in the stacked displacement time series (Figure S14a) is also observed in July, consistent with the timing of the creepmeters, followed by a decrease likely related to atmospheric noise. The delayed detection likely reflects the higher noise level of the Ismetpasa InSAR dataset and the lower signal amplitude of this event. Nevertheless, the inferred depth range remains broadly compatible with previous geodetic interpretations (Jolivet & Frank, 2020; Özdemir et al., 2025), suggesting that the detection is physically meaningful even if its temporal characterization is less precise.

More generally, the comparison with GNSS observations highlights the complementary strengths of the datasets. GNSS provides higher temporal resolution but sparse spatial sampling, whereas InSAR offers dense spatial coverage but limited temporal resolution. The matched filter approach leverages the spatial redundancy of InSAR to compensate for its lower temporal sampling, enabling the recovery of shallow, kilometer-scale events that may be only partially resolved by GNSS networks.

4.2.3 Synthesis across techniques

Importantly, no additional events are detected when lowering the PRP, suggesting that the current InSAR noise level likely prevents the identification of smaller, millimetric SSEs documented by creepmeters (e.g., mid-2018 along Ismetpasa; Figure S16a).

The overall consistency between the template-based detections and independent geodetic constraints indicates that the method successfully captures the first-order physical characteristics of shallow SSEs without requiring a full slip inversion. Differences in initiation times and relaxation times remain within the limits imposed by the temporal sampling and noise level of the InSAR data. These comparisons demonstrate that the geodetic matched filter approach provides a robust framework for systematic SSE detection while remaining consistent with high-resolution *in situ* observations. Nevertheless, when the signal-to-noise ratio allows it, a dedicated slip inversion would provide a more detailed characterization of the spatial distribution of slip and a refined estimate of the moment (Rousset et al., 2016; Neyrinck et al., 2024).

4.3 Slow slip events physical mechanisms

4.3.1 Structural and mechanical controls on shallow SSE occurrence

The shallow SSEs identified along the Izmit and Ismetpasa segments occur within fault sections that are already characterized by aseismic creep. On the Izmit segment, aseismic creep appears to be localized primarily downdip of the SSEs (Neyrinck et al., 2024), whereas along the Ismetpasa segment it is observed on both sides of the SSEs and possibly beneath them as well (Jolivet & Frank, 2020). This observation may indicate that surrounding persistent aseismic creep constitutes a necessary mechanical background for the occurrence of shallow SSEs. In rate-and-state friction frameworks, velocity-strengthening regions are typically associated with stable creep (Kaneko et al., 2013), but spatial heterogeneities within such regions may lead to conditionally stable behavior and the emergence of transient slip episodes (Wei et al., 2013). The fact that both Izmit and Ismetpasa host SSEs within creeping sections, while most other NAF segments do not, supports the hypothesis that a pre-existing aseismic slip regime may be a prerequisite for transient slow slip.

In addition to the presence of creep, both segments share a striking geological feature: the SSEs are systematically located within sedimentary basins. Along the Izmit segment, the detected events are confined within the Izmit basin (Figure 8a), whose downdip boundary lies at about two kilometers depth (Özalaybey et al., 2011). Along the Ismetpasa segment, the events are also located within a shallow sedimentary cover (Jolivet et al., 2023; Özdemir et al., 2025). Sedimentary basins are typically characterized by clay-rich, weak, and potentially overpressurized materials, which may favor stable or conditionally stable slip (Bürgmann, 2018).

The geological context of the NAF is complex, as the fault follows former suture zones separating distinct lithological units (Şengör et al., 2005). However, only two segments exhibit both shallow creep and recurrent SSEs, suggesting that lithological contrasts alone are insufficient to explain their occurrence. The spatial coincidence between SSEs and sedimentary basins instead points toward the importance of shallow material properties. Similar associations between shallow slow slip and sedimentary or altered materials have been documented along other continental strike-slip faults, including the Imperial and Superstition Hills faults in California (Materna et al., 2024; Vavra et al., 2024). These analogies suggest that the presence of compliant, clay-rich may promote frictional conditions favorable to transient aseismic slip.

4.3.2 Role of pore-fluid pressure

Elevated pore-fluid pressure likely plays a central role in the nucleation and evolution of the shallow SSEs identified along both the Izmit and Ismetpasa segments. High pore pressure reduces the effective normal stress acting on the fault, thereby lowering the shear stress required for slip and promoting aseismic deformation (Sibson, 1992). In creeping fault sections overlain by or within sedimentary basins, permeability contrasts, clay-rich lithologies, and fluid trapping may favor locally elevated pore pressures. Such conditions are commonly invoked to explain stable or conditionally stable slip behavior in both subduction zones and continental strike-slip faults (e.g. Bürgmann, 2018).

Theoretical and numerical studies have shown that fluid pressure variations can significantly modify slip stability in rate-and-state systems. Coupled hydromechanical models demonstrate that pore-pressure diffusion may generate slow slip pulses even in velocity-strengthening regimes, provided that effective normal stress is sufficiently reduced (Segall & Rice, 1995; Segall & Matthews, 1997; Liu & Rice, 2007; Heimisson et al., 2019). In particular, Heimisson et al. (2019) showed that poroelastic coupling can destabilize otherwise stable sliding and produce transient SSEs with durations and magnitudes comparable to those observed geodetically.

Dilatancy further modulates this behavior. During shear, fault zone dilatation reduces pore pressure locally, temporarily increasing effective normal stress and stabilizing slip. Subsequent fluid diffusion restores pore pressure, allowing slip to resume. This dilatancy–diffusion feedback has been proposed as a key mechanism governing episodic slow slip in subduction settings (Segall & Rice, 1995; Liu & Rice, 2007) and may similarly operate in shallow continental environments. The shallow depth of the detected events ($\leq 2\ km$) is consistent with zones where permeability heterogeneities and fluid circulation are expected to be strong, particularly within sedimentary basins.

Seasonal modulation of creep attributed to hydrological loading suggested by Li et al. (2023) on the San Andreas fault highlights the potential sensitivity of shallow fault slip to effective stress variations. Although no clear seasonal modulation of slip is resolved here, the fact that SSEs on the Izmit segment consistently occur in winter suggests that pressure transients may play a role in triggering the SSEs.

4.3.3 Moment-duration scaling

The detected SSEs fall within the moment-duration domain previously identified for shallow continental SSEs (Figure 9). When plotted on the scaling diagram adapted from Ide and Beroza (2023) and Materna et al. (2024), the Izmit and Ismetpasa events cluster within the so-called "hidden" region for subduction zones, corresponding to low-magnitude, short-duration events that are only detectable on strike-slip faults because of their shallow depth.

Their position on the diagram is consistent with moment magnitudes $M_w \sim 4-4.3$ and durations of days to a few weeks. These values align with observations from other continental creeping faults (Materna et al., 2024; Vavra et al., 2024) and suggest that shallow SSEs obey a scaling shifted from that of fast earthquakes and subduction SSEs. Although the limited number of events prevents robust scaling estimation, the clustering of the NAF SSEs within a narrow portion of the scaling space suggests that common mechanical conditions govern their occurrence. The similarity between Izmit and Ismetpasa, despite their different positions within the seismic cycle (post-1999 rupture versus $\sim 80\ years$ after the 1944 rupture), indicates that local frictional and hydromechanical properties may dominate over large-scale stress evolution in controlling shallow SSE behavior.

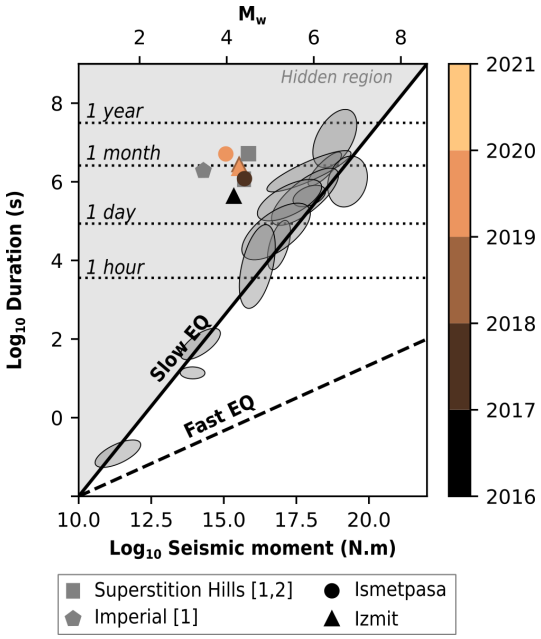

Figure 9. Moment-duration scaling plot modified from Ide and Beroza (2023) and Materna et al. (2024). Results from this study are shown by the colored circles and triangles. The references 1 and 2 used for the Imperial Valley results correspond to Materna et al. (2024) and Vavra et al. (2024), respectively. Gray ellipses correspond to estimates made on subduction zones (Ide & Beroza, 2023).

4.3.4 Implications for continental fault mechanics

Taken together, the observations support a conceptual model in which shallow SSEs preferentially develop on fault portions surrounded by creeping segments and within sedimentary basins, where frictional heterogeneity, compliant materials, and fluid effects combine to produce conditionally stable slip. Persistent aseismic surrounding creep may provide the background deformation necessary to load small velocity-weakening or conditionally stable patches, leading to recurrent transient slip.

The similarity of these features with those documented in California suggests that such structural and hydromechanical conditions may represent a common ingredient for shallow SSE occurrences worldwide. Expanding SSE catalogs using systematic approaches, such as the geodetic matched filter, will be essential to test whether this association between creep, sedimentary cover, and shallow slow slip holds across broader tectonic contexts.

5 Conclusion

The adaptation of the geodetic matched filter approach to InSAR time series enables the detection of shallow SSEs along continental strike-slip fault segments, under assumptions that are consistent with previous observational and modeling studies. Applied to two distinct creeping segments of the North Anatolian Fault, this method demonstrates its ability to automatically detect and characterize SSEs without requiring extensive post-processing or full slip inversions. Over the 2016-2021 period, we identify three events along the Izmit segment and two along the Ismetpasa segment, with moment magnitudes ranging from $M_w \sim 4$ to 4.4, compatible with previous estimates, all located

within the upper few kilometers of the fault interface. The geodetic matched filter provides a systematic screening tool for large InSAR datasets, guiding more detailed analyses when the signal-to-noise ratio permits. With the continuous increase in SAR acquisitions, improvements in automated InSAR processing, and the development of advanced post-processing techniques, such approaches open the possibility of systematically documenting aseismic transient deformation along continental faults over decadal time scales. Expanding SSE catalogs is essential for better constraining the kinematics and mechanics of shallow fault slip, improving our understanding of fault zone processes, and refining seismic hazard assessments in regions hosting creeping strike-slip faults.

Open Research Section

The FLATSIM data used in this study are available via doi: 10.24400/253171/FLATSIM2020 (`https://www.poleterresolide.fr/le-service-flatsim/`, Thollard et al. (2021)).

Conflict of Interest disclosure

The authors declare there are no conflicts of interest for this manuscript.

Acknowledgments

We thank Cécile Lasserre, Marie-Pierre Doin and Philippe Durand for stimulating discussions. The InSAR data is based on the FLATSIM service (doi: 10.24400/253171/FLATSIM2020), developed as part of the ForM@Ter Solid Earth data and services center and supported and operated by CNES. Creepmeters data come from the GAGE/UNAVCO dataset (`https://www.unavco.org/data/strain-seismic/creep-data/creep-data.html`). Baptiste Rousset has benefited funding for this study from the CNRS PNTS and the IdEx University of Strasbourg.

References

Akaike, H. (1974). A new look at the statistical model identification. *IEEE Transactions on Automatic Control*, *19*(6), 716-723. doi: 10.1109/TAC.1974.1100705

Ambraseys, N. N. (1970). Some characteristic features of the anatolian fault zone. *Tectonophysics*, *9*(2-3), 143–165.

Aslan, G., Lasserre, C., Cakir, Z., Ergintav, S., Özarpaci, S., Dogan, U., ... Renard, F. (2019). Shallow creep along the 1999 izmit earthquake rupture (turkey) from gps and high temporal resolution interferometric synthetic aperture radar data (2011–2017). *Journal of Geophysical Research: Solid Earth*, *124*(2), 2218–2236.

Avouac, J.-P. (2015). From geodetic imaging of seismic and aseismic fault slip to dynamic modeling of the seismic cycle. *Annual Review of Earth and Planetary Sciences*, *43*(1), 233–271.

Barka, A. (1999). The 17 august 1999 izmit earthquake. *Science*, *285*(5435), 1858–1859.

Bekaert, D., Segall, P., Wright, T. J., & Hooper, A. J. (2016). A network inversion filter combining gnss and insar for tectonic slip modeling. *Journal of Geophysical Research: Solid Earth*, *121*(3), 2069–2086.

Bilham, R., Ozener, H., Mencin, D., Dogru, A., Ergintav, S., Cakir, Z., ... others (2016). Surface creep on the north anatolian fault at ismetpasa, turkey, 1944–2016. *Journal of Geophysical Research: Solid Earth*, *121*(10), 7409–7431.

Bürgmann, R. (2018). The geophysics, geology and mechanics of slow fault slip. *Earth and Planetary Science Letters*, *495*, 112–134.

Cakir, Z., Akoglu, A. M., Belabbes, S., Ergintav, S., & Meghraoui, M. (2005). Creeping along the ismetpasa section of the north anatolian fault (western turkey): Rate and extent from insar. *Earth and Planetary Science Letters*, *238*(1-2), 225–234.

Çakir, Z., Ergintav, S., Özener, H., Dogan, U., Akoglu, A. M., Meghraoui, M., & Reilinger, R. (2012). Onset of aseismic creep on major strike-slip faults. *Geology*, *40*(12), 1115–1118.

Costantino, G., Giffard-Roisin, S., Dalla Mura, M., & Socquet, A. (2024). Denoising of geodetic time series using spatiotemporal graph neural networks: application to slow slip event extraction. *IEEE Journal of Selected Topics in Applied Earth Observations and Remote Sensing*.

Doin, M.-P., Lodge, F., Guillaso, S., Jolivet, R., Lasserre, C., Ducret, G., ... Pinel, V. (2011). Presentation of the small baselin nsbas processing chain on a case example: The etan deformation monitoring from 2003 to 2010 using envisat data. In *Fringe symposium*.

Dragert, H., Wang, K., & James, T. S. (2001). A silent slip event on the deeper cascadia subduction interface. *Science*, *292*(5521), 1525–1528.

Emre, Ö., Duman, T. Y., Özalp, S., Şaroğlu, F., Olgun, Ş., Elmacı, H., & Çan, T. (2018). Active fault database of turkey. *Bulletin of Earthquake Engineering*, *16*(8), 3229–3275.

Gualandi, A., & Liu, Z. (2021). Variational bayesian independent component analysis for insar displacement time-series with application to central california, usa. *Journal of Geophysical Research: Solid Earth*, *126*(4), e2020JB020845.

Gualandi, A., Serpelloni, E., & Belardinelli, M. E. (2016). Blind source separation problem in gps time series. *Journal of Geodesy*, *90*, 323–341. doi: 10.1007/s00190-015-0875-4

Hawthorne, J. C., & Rubin, A. M. (2013). Short-time scale correlation between slow slip and tremor in cascadia. *Journal of Geophysical Research: Solid Earth*, *118*(3), 1316–1329.

Heimisson, E. R., Dunham, E. M., & Almquist, M. (2019). Poroelastic effects destabilize mildly rate-strengthening friction to generate stable slow slip pulses. *Journal of the Mechanics and Physics of Solids*, *130*, 262–279.

Hirose, H., & Obara, K. (2005). Repeating short-and long-term slow slip events with deep tremor activity around the bungo channel region, southwest japan. *Earth, planets and space*, *57*(10), 961–972.

Ide, S., & Beroza, G. C. (2023). Slow earthquake scaling reconsidered as a boundary between distinct modes of rupture propagation. *Proceedings of the National Academy of Sciences*, *120*(32), e2222102120.

Jara, J., Jolivet, R., Socquet, A., Comte, D., & Norabuena, E. (2024). Detection of slow slip events along the southern peru-northern chile subduction zone. *Seismica*, *3*(1), 17567–17579.

Jasir, M., Sreejith, K., Agrawal, R., & Begum, S. (2024). Application of singular spectrum analysis to insar time-series for constraining the post-seismic deformation due to moderate magnitude earthquakes: the case of 2019 m w 6 mirpur earthquake, nw himalaya. *Geophysical Journal International*, *239*(1), 637–645.

Jolivet, R., & Frank, W. (2020). The transient and intermittent nature of slow slip. *AGU Advances*, *1*(1), e2019AV000126.

Jolivet, R., Jara, J., Dalaison, M., Rouet-Leduc, B., Özdemir, A., Dogan, U., ... Dubernet, P. (2023). Daily to centennial behavior of aseismic slip along the central section of the north anatolian fault. *Journal of Geophysical Research: Solid Earth*, *128*(7), e2022JB026018.

Kaneko, Y., Fialko, Y., Sandwell, D. T., Tong, X., & Furuya, M. (2013). Interseismic deformation and creep along the central section of the north anatolian fault (turkey): Insar observations and implications for rate-and-state friction

properties. *Journal of Geophysical Research: Solid Earth*, *118*(1), 316–331.

Karabulut, H. (2025). High-resolution p-wave tomography of the 1999 izmit and düzce earthquake rupture zones. *Geophysical Journal International*, *241*(2), 986–1008.

Kositsky, A., & Avouac, J.-P. (2010). Inverting geodetic time series with a principal component analysis-based inversion method. *Journal of Geophysical Research: Solid Earth*, *115*(B3).

Laske, G., Masters, G., Ma, Z., & Pasyanos, M. (2013). Update on crust1. 0—a 1-degree global model of earth's crust. In *Geophysical research abstracts* (Vol. 15, p. 2658).

Li, Y., Bürgmann, R., & Taira, T. (2023). Spatiotemporal variations of surface deformation, shallow creep rate, and slip partitioning between the san andreas and southern calaveras fault. *Journal of Geophysical Research: Solid Earth*, *128*(1), e2022JB025363.

Linde, A. T., Gladwin, M. T., Johnston, M. J., Gwyther, R. L., & Bilham, R. G. (1996). A slow earthquake sequence on the san andreas fault. *Nature*, *383*(6595), 65–68.

Liu, Y., & Rice, J. R. (2007). Spontaneous and triggered aseismic deformation transients in a subduction fault model. *Journal of Geophysical Research*, *112*, B09404. doi: 10.1029/2007JB004930

Marill, L., Marsan, D., Rousset, B., & Socquet, A. (2024). Geodetic matched filter slow slip event detection along the northern japan subduction zones. *Journal of Geophysical Research: Solid Earth*, *129*(9), e2024JB029342.

Materna, K., Bürgmann, R., Lindsay, D., Bilham, R., Herring, T., Crowell, B., & Szeliga, W. (2024). Shallow slow slip events in the imperial valley with along-strike propagation. *Geophysical Research Letters*, *51*(12), e2023GL108089.

Maubant, L., Pathier, E., Daout, S., Radiguet, M., Doin, M.-P., Kazachkina, E., ... Walpersdorf, A. (2020). Independent component analysis and parametric approach for source separation in insar time series at regional scale: Application to the 2017–2018 slow slip event in guerrero (mexico). *Journal of Geophysical Research: Solid Earth*, *125*(3), e2019JB018187.

Neyrinck, E., Rousset, B., Doubre, C., Rivera, L., Lasserre, C., Doin, M.-P., ... others (2024). The slow slip event cycle along the izmit segment of the north anatolian fault. *Earth and Planetary Science Letters*, *648*, 119104.

Nishimura, T. (2014). Short-term slow slip events along the ryukyu trench, southwestern japan, observed by continuous gnss. *Progress in Earth and Planetary Science*, *1*(22), 1–13. Retrieved from `https://doi.org/10.1186/s40645-014-0022-5` doi: 10.1186/s40645-014-0022-5

Okada, Y., & Nishimura, T. (2023). Systematic detection of short-term slow slip events in southcentral alaska. *Geophysical Research Letters*, *50*(17), e2023GL104901.

Okada, Y., Nishimura, T., Tabei, T., Matsushima, T., & Hirose, H. (2022). Development of a detection method for short-term slow slip events using gnss data and its application to the nankai subduction zone. *Earth, Planets and Space*, *74*(1), 1–18.

Özalaybey, S., Zor, E., Ergintav, S., & Tapırdamaz, M. C. (2011). Investigation of 3-d basin structures in the izmit bay area (turkey) by single-station microtremor and gravimetric methods. *Geophysical Journal International*, *186*(2), 883–894.

Özdemir, A., Jara, J., Doğan, U., Jolivet, R., Çakir, Z., Nocquet, J.-M., ... Bilham, R. (2025). Detecting millimetric slow slip events along the north anatolian fault with gnss. *Geophysical Research Letters*, *52*(10), e2024GL111428.

Riel, B., Simons, M., Agram, P., & Zhan, Z. (2014). Detecting transient signals in geodetic time series using sparse estimation techniques. *Journal of Geophysical Research: Solid Earth*, *119*(6), 5140–5160.

Rouet-Leduc, B., Jolivet, R., Dalaison, M., Johnson, P. A., & Hulbert, C. (2021).

Autonomous extraction of millimeter-scale deformation in insar time series using deep learning. *Nature communications*, *12*(1), 6480.

Rousset, B., Bürgmann, R., & Campillo, M. (2019). Slow slip events in the roots of the san andreas fault. *Science advances*, *5*(2), eaav3274.

Rousset, B., Campillo, M., Lasserre, C., Frank, W. B., Cotte, N., Walpersdorf, A., ... Kostoglodov, V. (2017). A geodetic matched filter search for slow slip with application to the mexico subduction zone. *Journal of Geophysical Research: Solid Earth*, *122*(12), 10–498.

Rousset, B., Jolivet, R., Simons, M., Lasserre, C., Riel, B., Milillo, P., ... Renard, F. (2016). An aseismic slip transient on the north anatolian fault. *Geophysical Research Letters*, *43*(7), 3254–3262.

Segall, P., & Matthews, M. (1997). Time dependent inversion of geodetic data. *Journal of Geophysical Research*, *102*(B10), 22,391–22,409. doi: 10.1029/97JB01795

Segall, P., & Rice, J. R. (1995). Dilational fault slip and earthquake sequence modeling. *Journal of Geophysical Research*, *100*(B11), 22155–22163. doi: 10.1029/95JB02403

Şengör, A., Tüysüz, O., Imren, C., Sakınç, M., Eyidoğan, H., Görür, N., ... Rangin, C. (2005). The north anatolian fault: A new look. *Annu. Rev. Earth Planet. Sci.*, *33*(1), 37–112.

Sibson, R. (1992). Implications of fault-valve behaviour for rupture nucleation and recurrence. *Tectonophysics*, *211*(1), 283-293. doi: https://doi.org/10.1016/0040-1951(92)90065-E

Stein, R. S., Barka, A. A., & Dieterich, J. H. (1997). Progressive failure on the north anatolian fault since 1939 by earthquake stress triggering. *Geophysical Journal International*, *128*(3), 594–604.

Steinbrugge, K. V., Zacher, E. G., Tocher, D., Whitten, C., & Claire, C. (1960). Creep on the san andreas fault. *Bulletin of the Seismological Society of America*, *50*(3), 389–415.

Thollard, F., Clesse, D., Doin, M.-P., Donadieu, J., Durand, P., Grandin, R., ... others (2021). Flatsim: The form@ ter large-scale multi-temporal sentinel-1 interferometry service. *Remote Sensing*, *13*(18), 3734.

Vavra, E. J., Fialko, Y., Rockwell, T., Bilham, R., Štěpančíková, P., Stemberk, J., ... Stemberk, J. (2024). Characteristic slow-slip events on the superstition hills fault, southern california. *Geophysical Research Letters*, *51*(12), e2023GL107244.

Walwer, D., Gonzalez-Santana, J., Wauthier, C., Calais, E., & Ghil, M. (2025). Multichannel singular spectrum analysis (m-ssa) of insar datasets: data-adaptive interpolation and decomposition of sentinel-1 time series at pacaya volcano, guatemala. *Geophysical Journal International*, ggaf257.

Wei, M., Kaneko, Y., Liu, Y., & McGuire, J. J. (2013). Episodic fault creep events in california controlled by shallow frictional heterogeneity. *Nature geoscience*, *6*(7), 566–570.

Zhu, L., & Rivera, L. A. (2002). A note on the dynamic and static displacements from a point source in multilayered media. *Geophysical Journal International*, *148*(3), 619–627.

Supporting Information for "Automated Detection of Slow Slip Events from InSAR: Application to the North Anatolian Fault"

Estelle Neyrinck[1], Baptiste Rousset[1], Cécile Doubre[1], Luis Rivera[1]

[1]ITES, CNRS, Université de Strasbourg, Strasbourg, France

Contents of this file

1. Figures S1 to S16

Introduction

The supplementary materials contain 16 figures in this file, as supplementary information of the main article.

References

Bilham, R., Ozener, H., Mencin, D., Dogru, A., Ergintav, S., Cakir, Z., ... others (2016). Surface creep on the north anatolian fault at ismetpasa, turkey, 1944–2016. *Journal of Geophysical Research: Solid Earth*, *121*(10), 7409–7431.

Emre, Ö., Duman, T. Y., Özalp, S., Şaroğlu, F., Olgun, Ş., Elmacı, H., & Çan, T. (2018). Active fault database of turkey. *Bulletin of Earthquake Engineering*, *16*(8), 3229–3275.

Karabulut, H. (2025). High-resolution p-wave tomography of the 1999 izmit and düzce

earthquake rupture zones. *Geophysical Journal International*, *241*(2), 986–1008.

Laske, G., Masters, G., Ma, Z., & Pasyanos, M. (2013). Update on crust1. 0—a 1-degree global model of earth's crust. In *Geophysical research abstracts* (Vol. 15, p. 2658).

Neyrinck, E., Rousset, B., Doubre, C., Rivera, L., Lasserre, C., Doin, M.-P., ... others (2024). The slow slip event cycle along the izmit segment of the north anatolian fault. *Earth and Planetary Science Letters*, *648*, 119104.

Özalaybey, S., Zor, E., Ergintav, S., & Tapırdamaz, M. C. (2011). Investigation of 3-d basin structures in the izmit bay area (turkey) by single-station microtremor and gravimetric methods. *Geophysical Journal International*, *186*(2), 883–894.

Rousset, B., Jolivet, R., Simons, M., Lasserre, C., Riel, B., Milillo, P., ... Renard, F. (2016). An aseismic slip transient on the north anatolian fault. *Geophysical Research Letters*, *43*(7), 3254–3262.

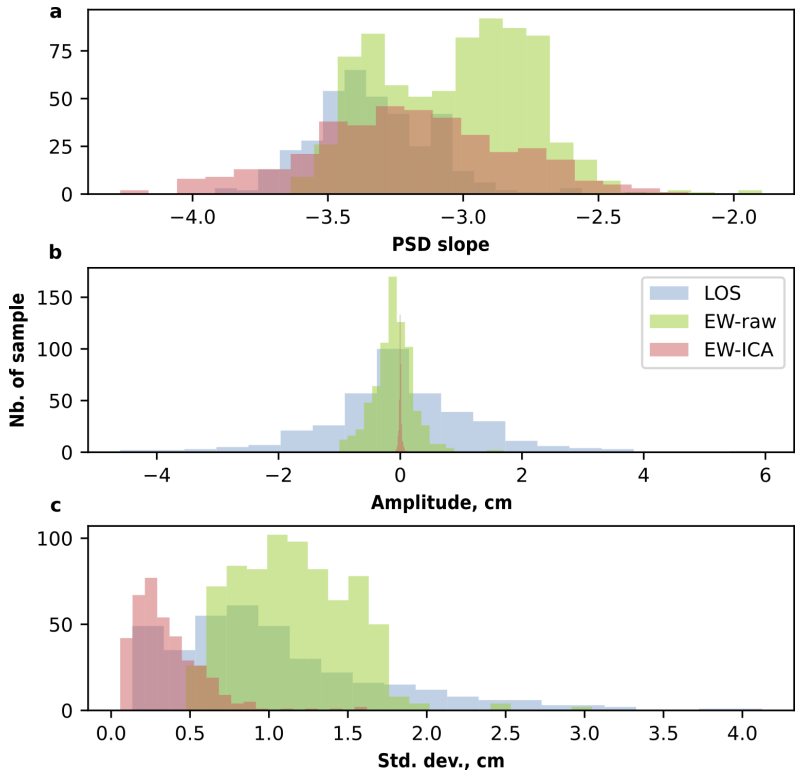

Figure S1. For the three datasets covering the Izmit segment, histograms of the (a) power spectral density (PSD) slope, (b) amplitude and (c) standard deviation of the real InSAR displacement time series. The blue, green and red colors correspond to noise contents from the Line-Of-Sight (LOS) displacement time series of the ascending track $A058$, the East-West (EW) displacement time series from the horizontal-vertical decomposition of the tracks $A058 - D138$ and the EW displacement time series after post-processing steps detailed in (Neyrinck et al., 2024) within the Izmit basin, respectively. The boxes used to compute those features are located within the area located between longitudes $30.0 - 30.6°E$ and latitudes $40.0 - 40.6°N$.

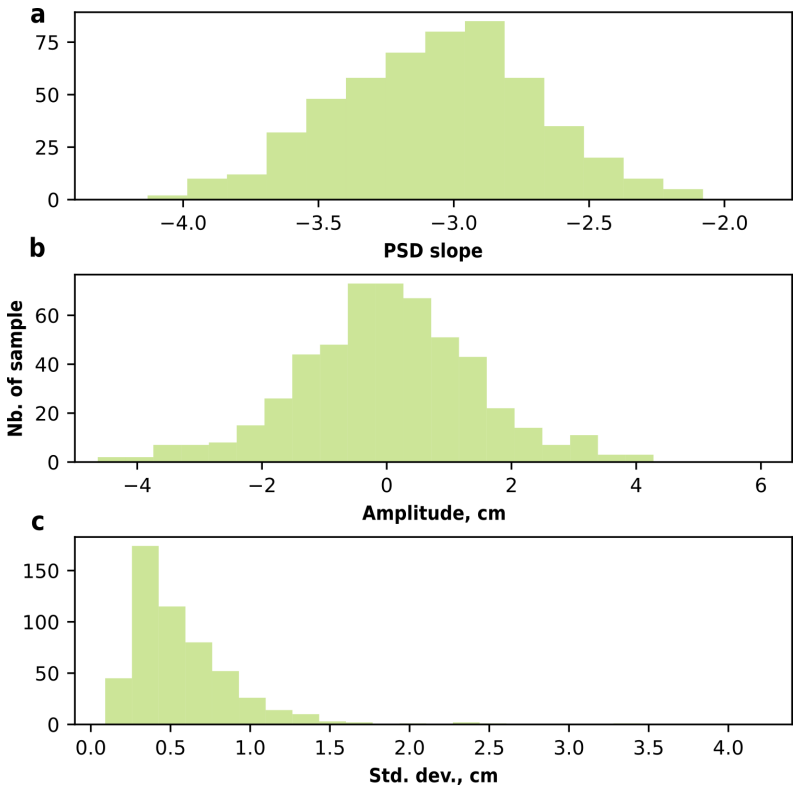

Figure S2. Histograms of the (a) PSD slope, (b) amplitude and (c) standard deviation of the real InSAR noise gathered from the Ismetpasa East-West displacement time series from the horizontal-vertical decomposition of the tracks $A087 - D065$. The boxes used to compute those features are located within the area longitudes $32.4 - 33.2$°E - latitudes $40.2 - 41.6$°N.

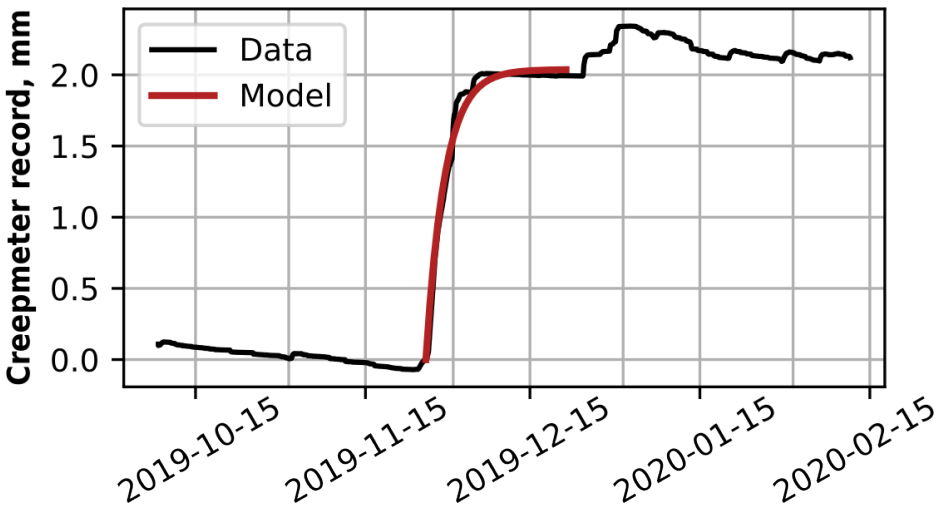

Figure S3. Creepmeter record at Seller (longitude 29.9720°E - latitude 40.7209°N) during the 2019 event. The red line corresponds to the fit based on the equation $s(t_1) = m(1 - e^{-\frac{t_1}{\tau}})$, with $m = 2.04mm$ and $\tau = 3.44days$. Creepmeters data come from the GAGE/UNAVCO dataset (`https://www.unavco.org/data/strain-seismic/creep-data/creep-data.html`).

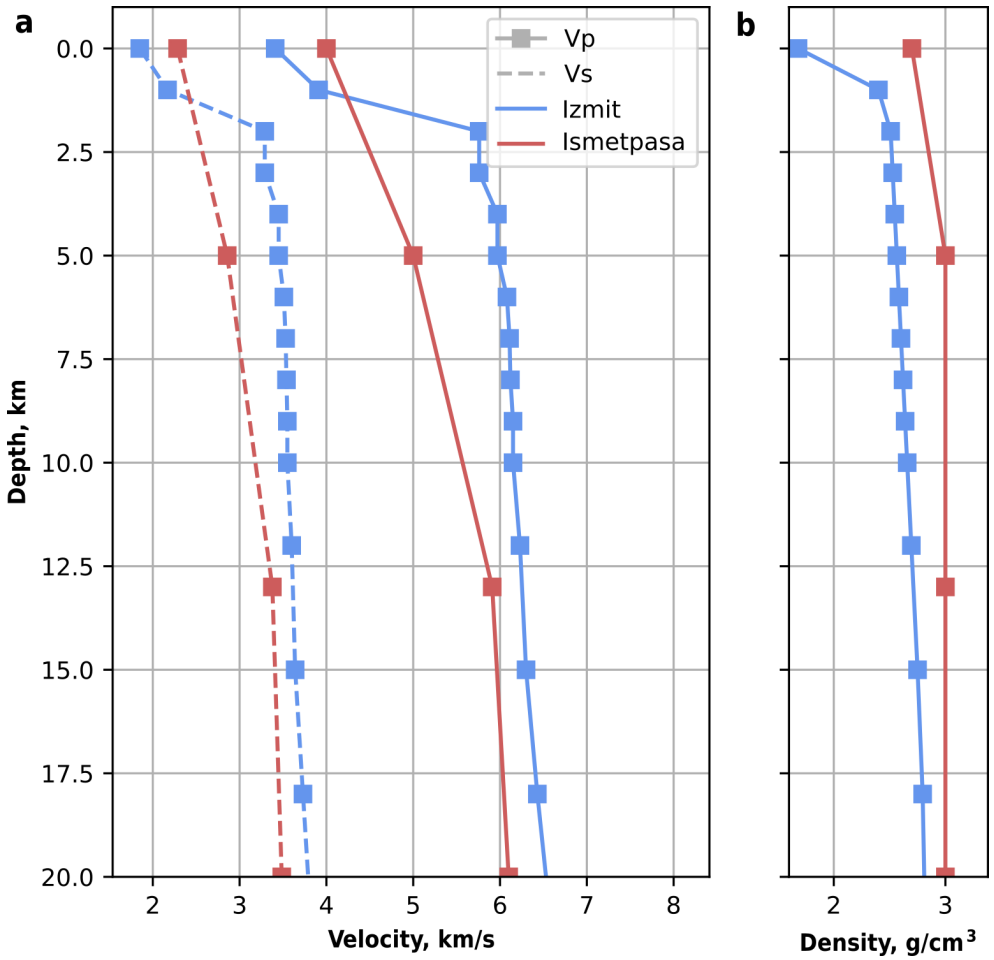

Figure S4. (a) P-wave velocity Vp , S-wave velocity Vs and (b) density ρ values used for the Green's functions computation for a stratified medium. Blue and red colors correspond to the velocities/densities at the Izmit and Ismetpasa segments, respectively. Along the Izmit segment, Vp and Vs values come from Karabulut (2025), ρ values from the surface down to $1.5km$-depth come from Özalaybey et al. (2011), and the other values of ρ are chosen according to Crust 1.0 (Laske et al., 2013). Along the Ismetpasa segment, all of the velocities/densities come from the model published by Rousset et al. (2016).

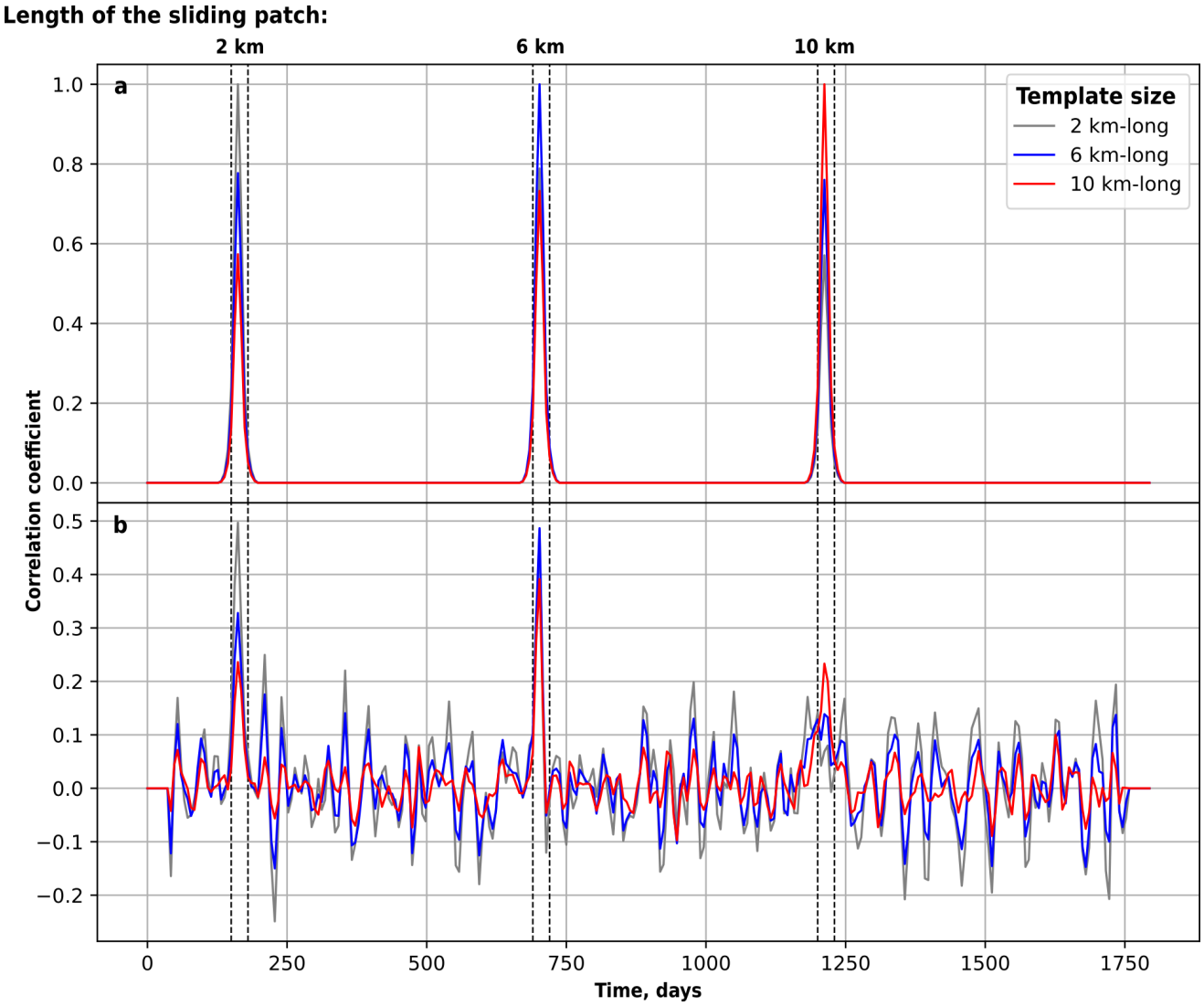

Figure S6. Effects of the patch size on the correlation coefficient. The correlation function is computed with a displacement time series cube of $300 dates$ containing three shallow SSEs located at depth $500m$ and with $M_w 4.8$, computed using three different sliding patch lengths: $2km$, $6km$ and $10km$. The width of the sliding patch is fixed of about $1km$. The periods affected by a SSE are limited by the vertical dotted lines. The curves show the correlation coefficients obtained by using three different template lengths ($2km$, $6km$ and $10km$). Sum of the correlation functions for synthetic displacement time series (a) without noise and (b) with realistic noise.

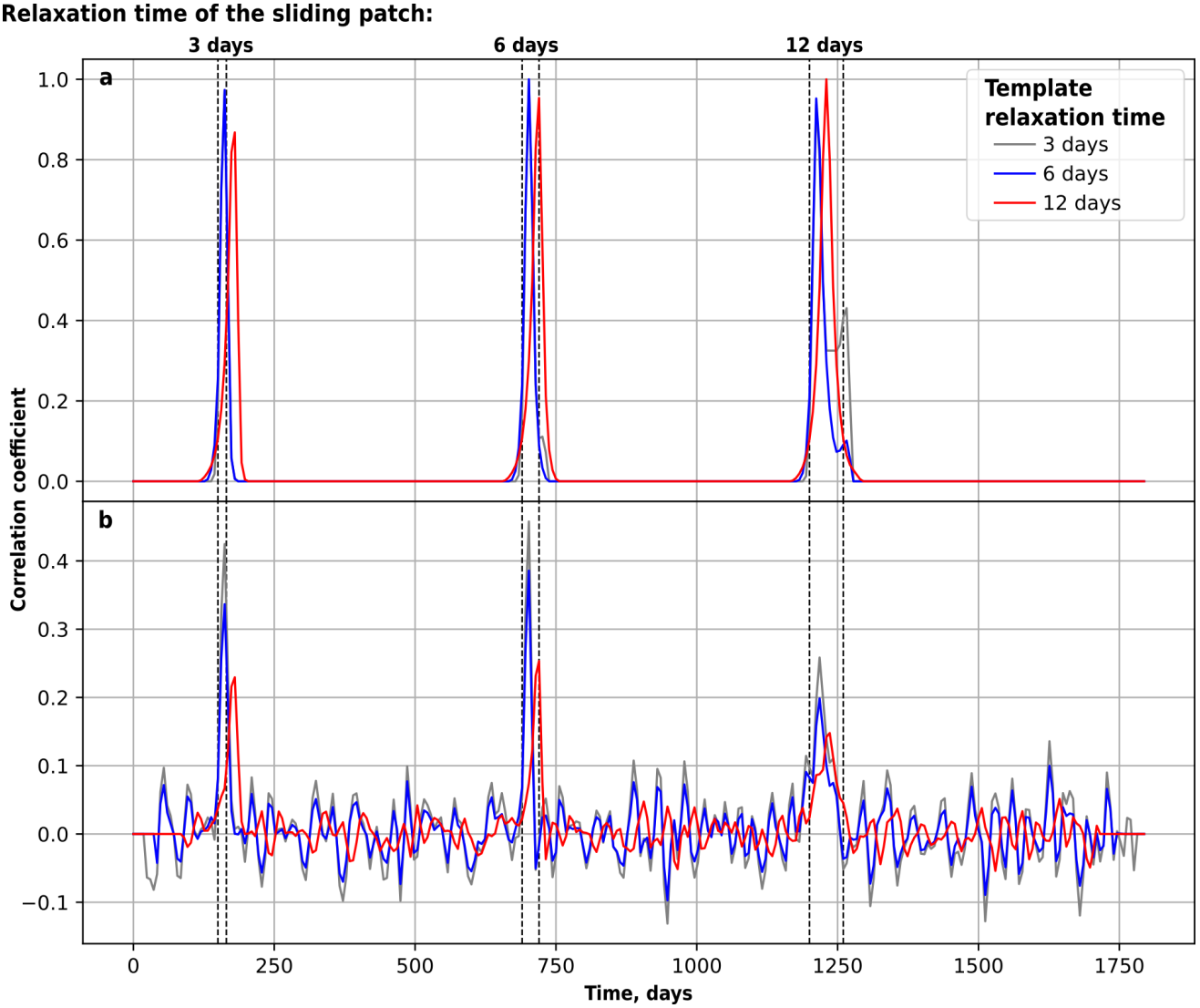

Figure S7. Effects of the relaxation time on the correlation coefficient. The correlation function is computed with a displacement time series cube of 300$dates$ containing three shallow SSEs located at depth 500m and with M_w4.8, computed using three different relaxation time: 3$days$, 6$days$ and 12$days$. The periods affected by a SSE are limited by the vertical dotted lines. The curves show the sum of the correlation functions computed by using the three previous relaxation time for the template. Sum of the correlation functions for synthetic displacement time series (a) without noise and (b) with realistic noise.

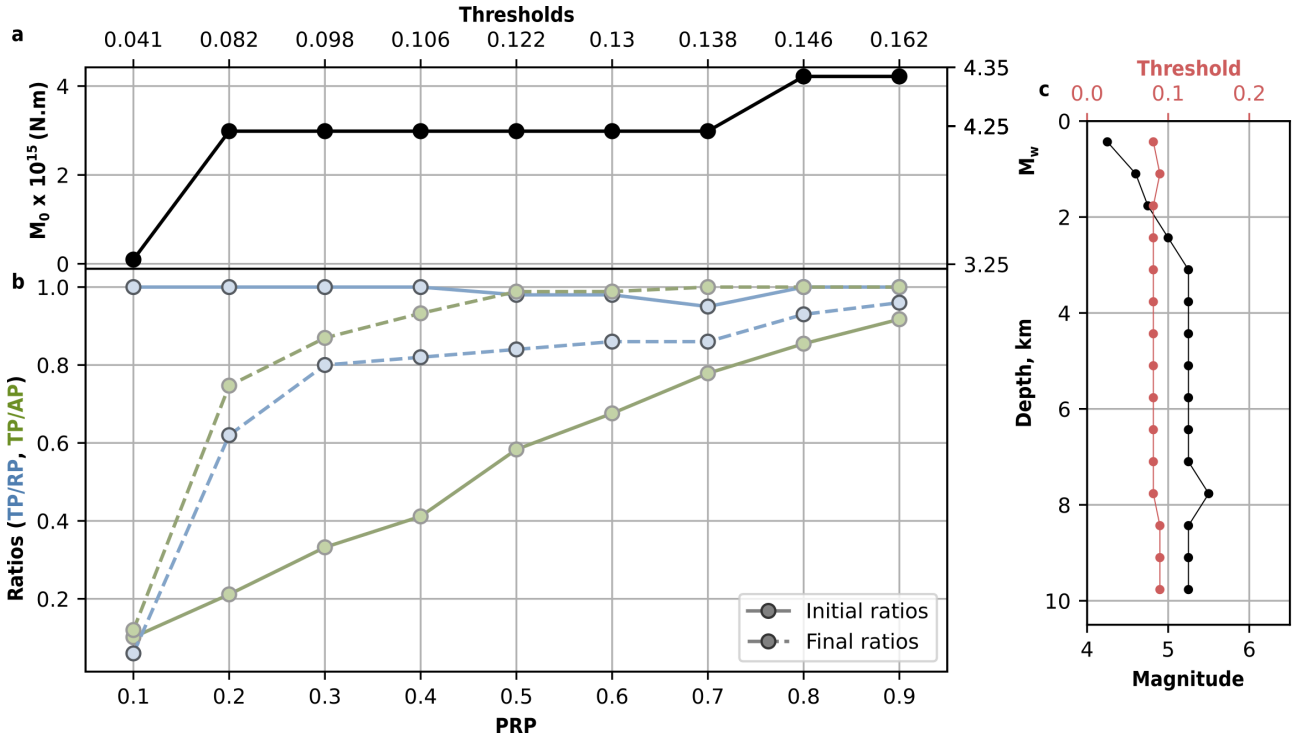

Figure S8. (a) Minimum moments M_0 (and corresponding magnitudes M_w, respectively) detected as a function of the precision-recall product (PRP). (b) TP/RP and TP/AP ratios as a function of PRP, shown in blue and green, respectively. TP stands for true positive detections, RP for real positive detections and AP for all the positive detections. Solid and dotted lines correspond to the ratios before and after the validation step. (c) Minimum magnitudes (black) and thresholds (pink) relative to $PRP \geq 0.2$ as a function of depth.

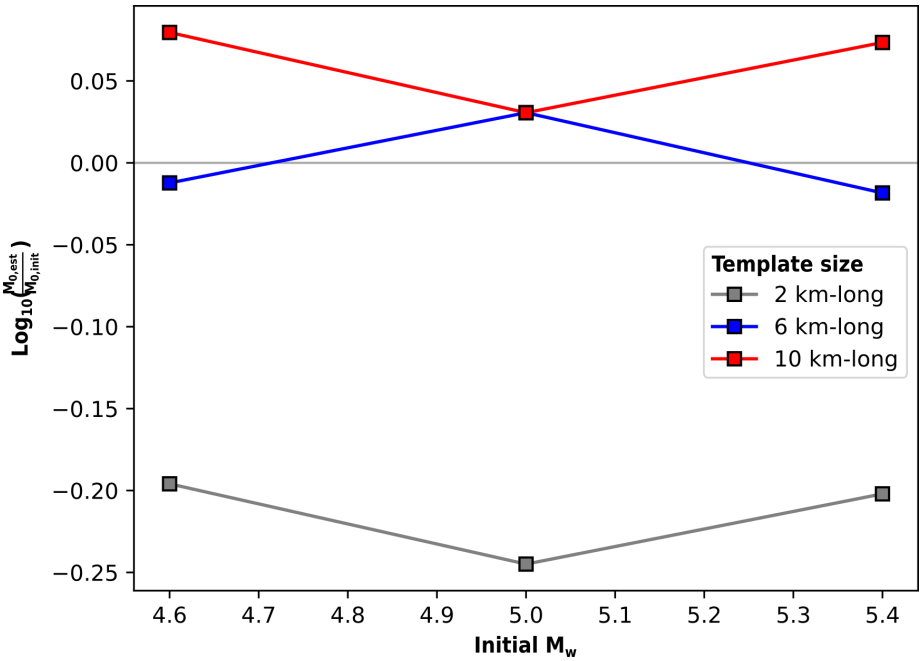

Figure S9. Comparison of the magnitude estimates during the characterization of the SSEs (*Module 3* – Figure 1d) and the real one chosen to build the synthetic displacement time series, related to the size of the template patch. A displacement time series cube of 300$dates$ including three shallow SSEs (depth 500m) are used for this test, without synthetic noise. The three SSEs have three different magnitudes but a similar sliding patch size of 6km-long and 1km-deep. From the first to the last event, the magnitude is 4.6, 5.0 and 5.4. Three analysis (detection + characterization) are done by using three different lengths of the template patch: 2km, 6km and 10km. The lines show the log of the ratio of the magnitude estimates and to the initial magnitude, obtained with three different template patch.

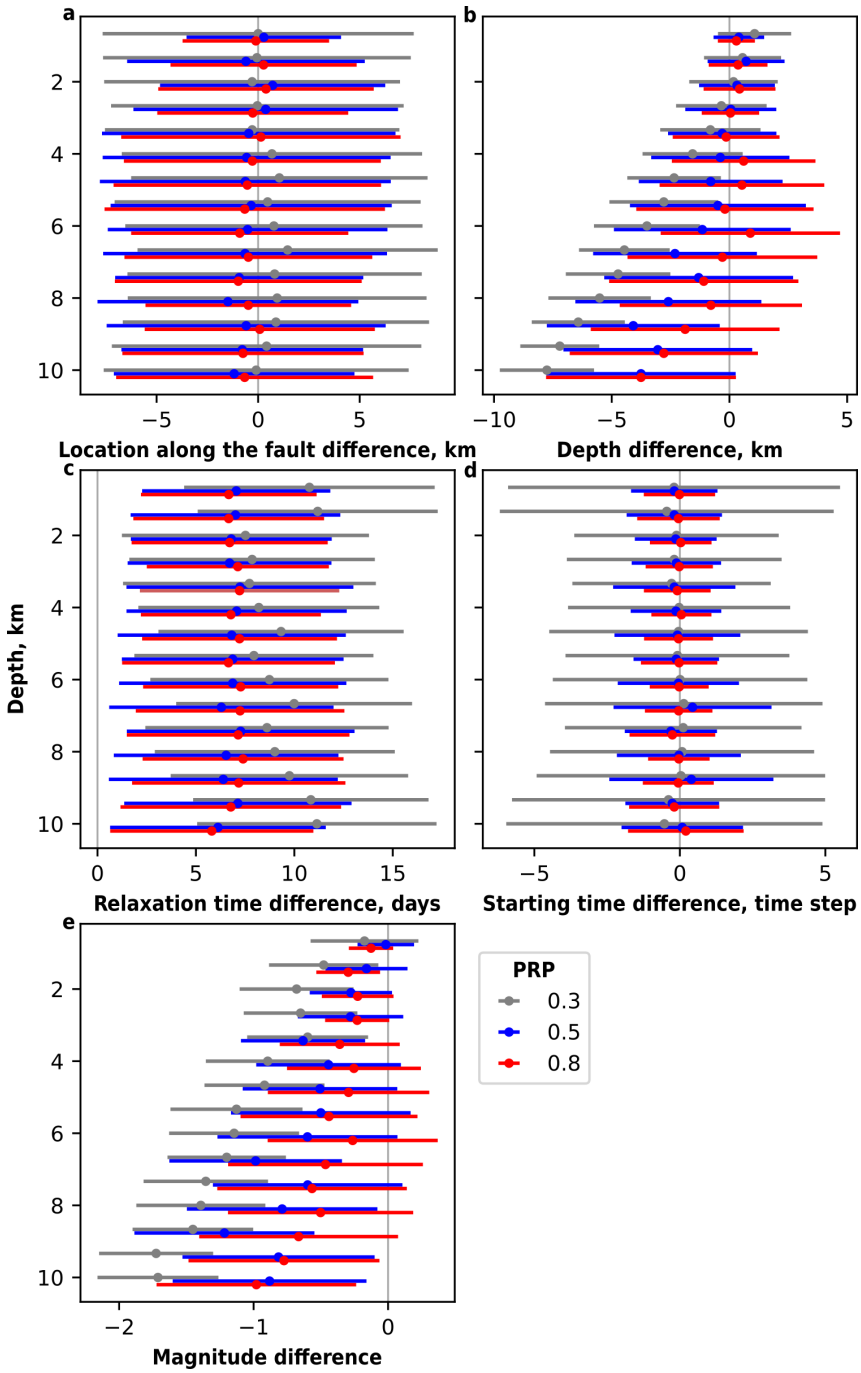

Figure S10. Estimates errors during the characterization of the detected SSEs. These errors are computed using a synthetic displacement time series made of 100 events, as explained in the main article. (a-b) Differences between the (a) location along the fault and (b) the depth of the sliding patch. (c-d) Differences between the (c) relaxation time and (b) starting time of the SSEs. (e) Differences between the magnitudes of the SSEs.

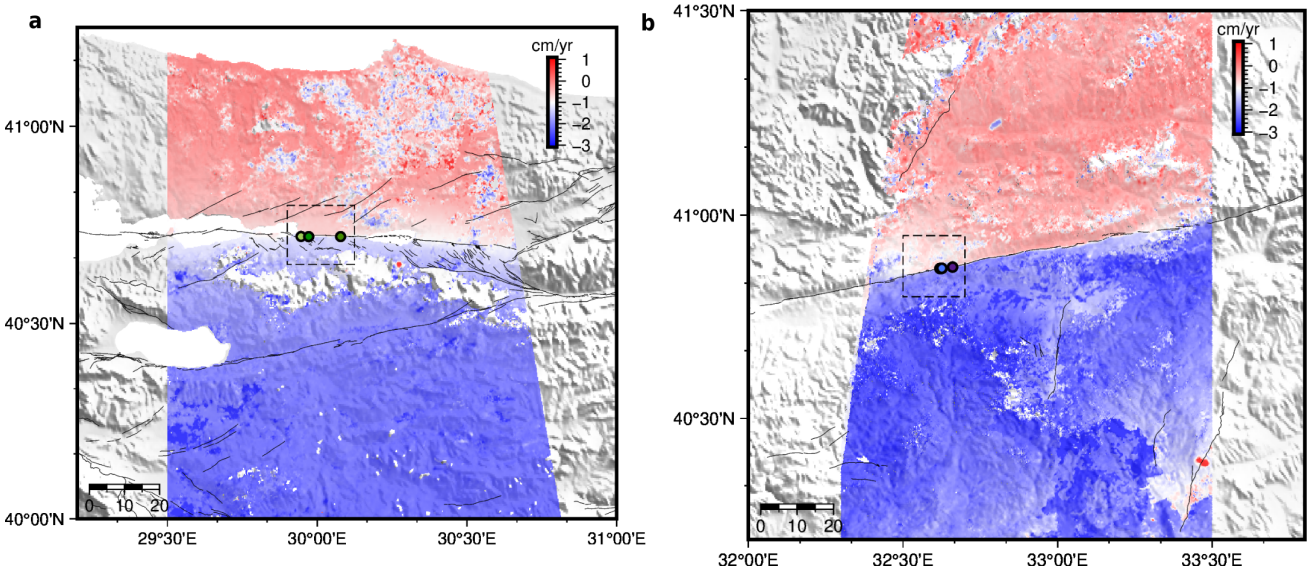

Figure S11. Mean East-West velocity maps after GNSS referencing covering the (a) Izmit and (b) Ismetpasa segments. The red and blue pixels correspond to eastward and westward motion, respectively. The fault network from Emre et al. (2018) is represented by the black lines. The creepmeters are shown by the colored circles (Bilham et al., 2016). The dashed rectangles show the cropped area surrounding the segments affected by SSEs, and used for the application of the geodetic matched filter approach. A zoom on the cropped areas is shown figure S12.

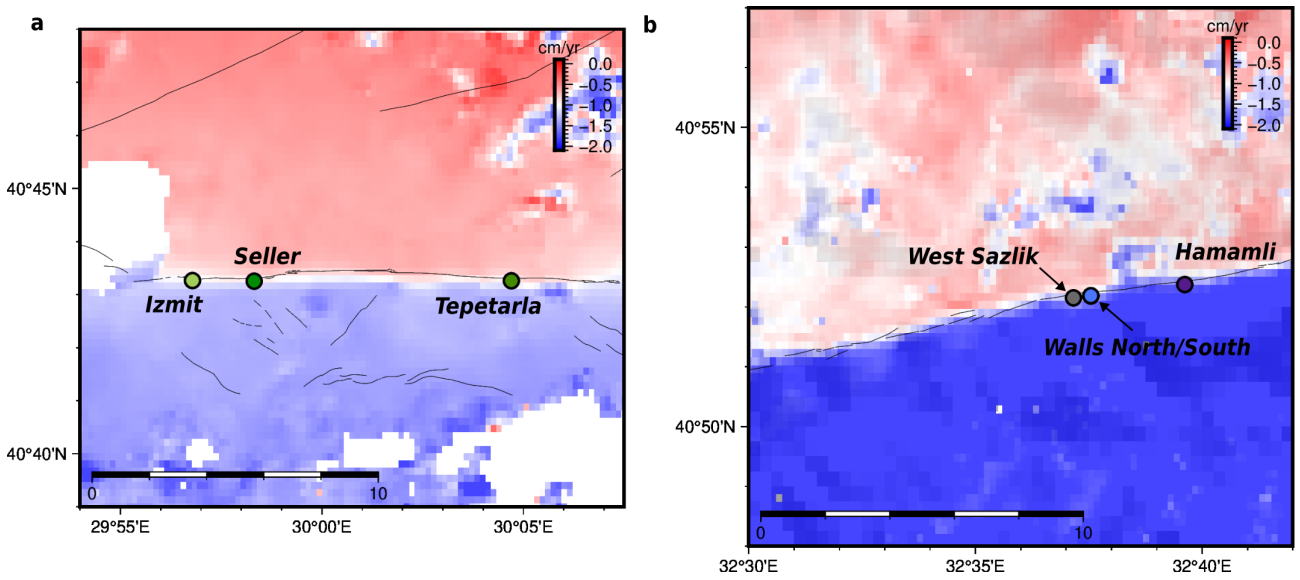

Figure S12. Mean East-West velocity maps after GNSS referencing covering the (a) Izmit and (b) Ismetpasa segments, focused on the cropped areas shown figure S11.

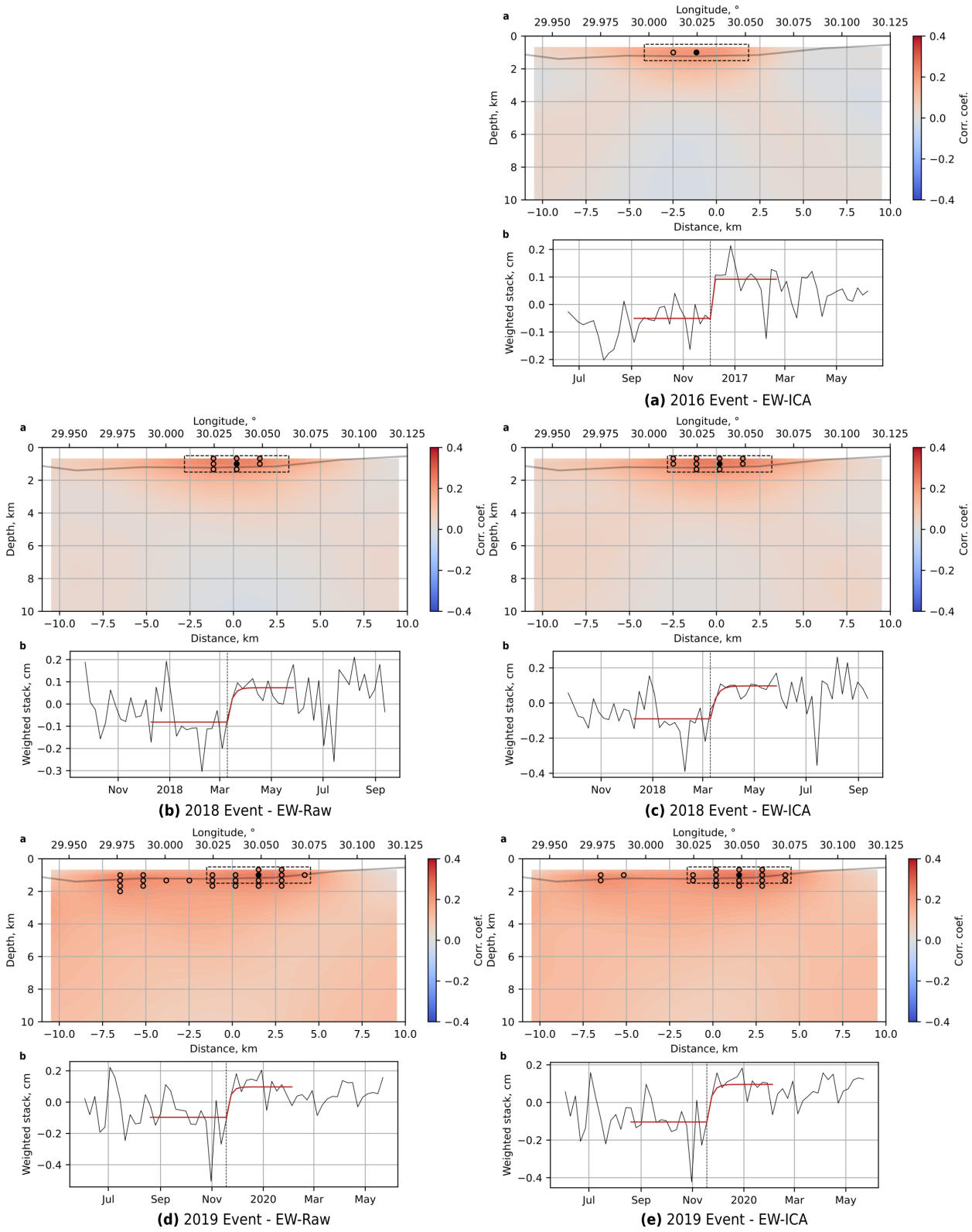

Figure S13. Final SSE detections along the Izmit segment.

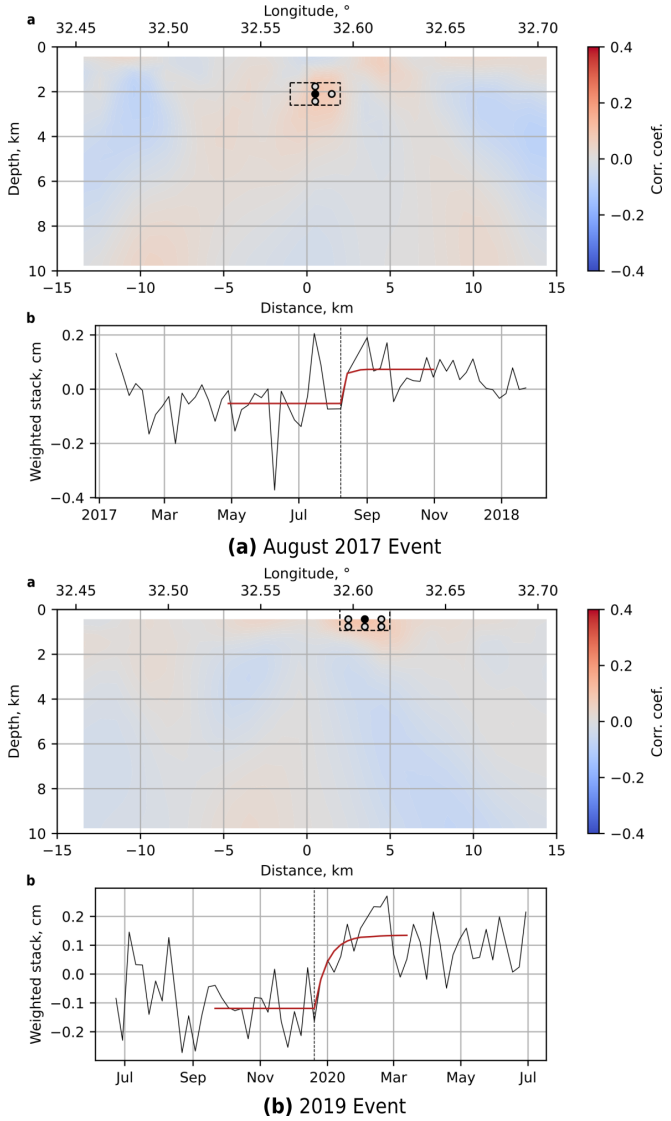

Figure S14. Final SSE detections along the Ismetpasa segment.

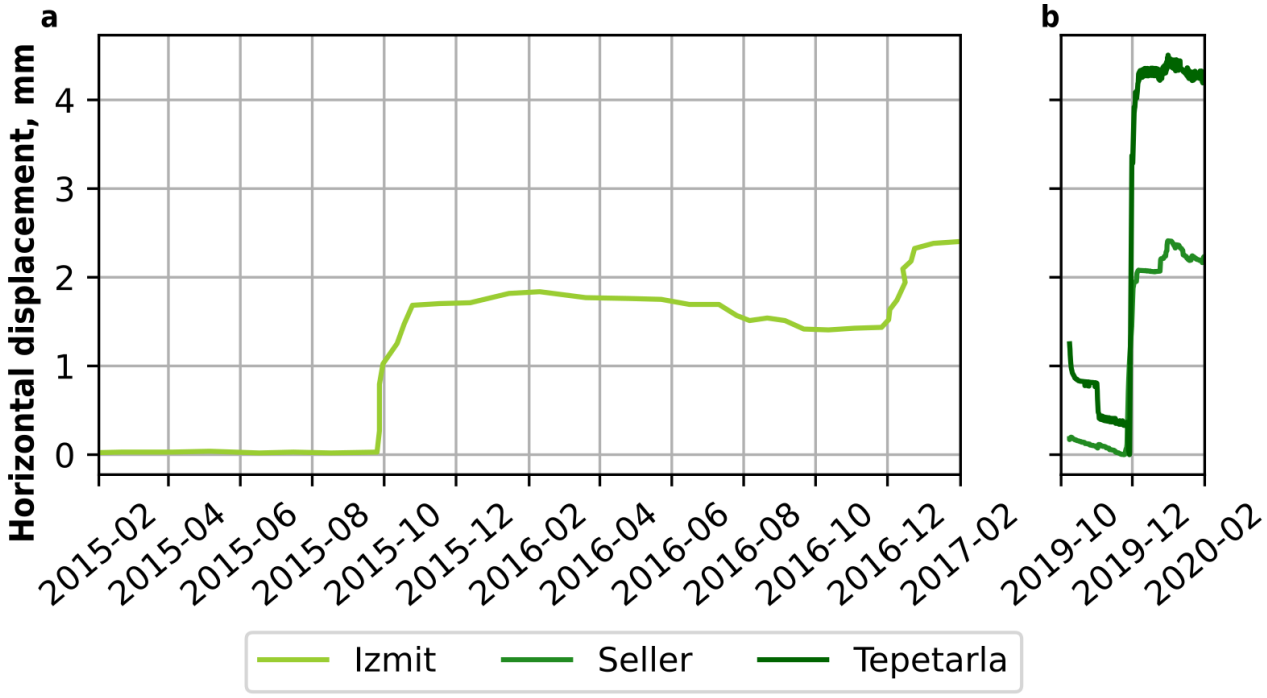

Figure S15. Creepmeters records along the Izmit segment.

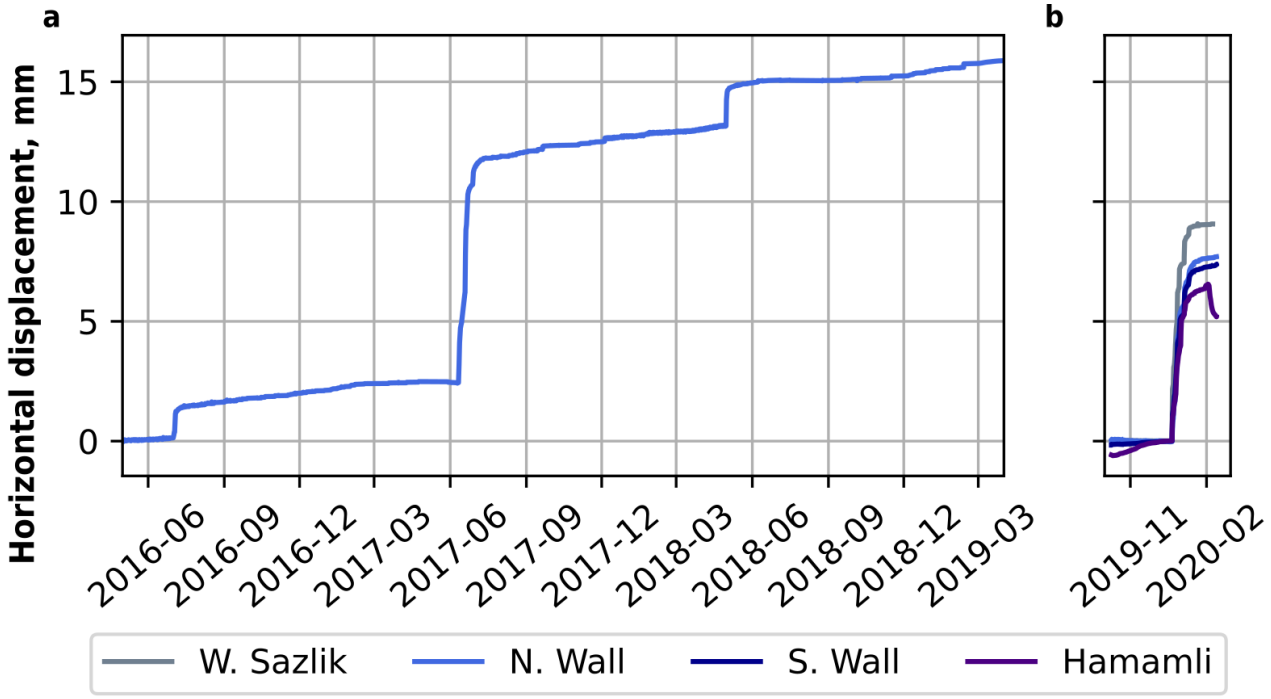

Figure S16. Creepmeters records along the Ismetpasa segment.